A Vulnerable Subtype of Dopaminergic Neurons Drives Early Motor Deficits in Parkinson's Disease

Akira Fushiki[1,2,9]*, David Ng[2], Zachary R. Lewis[1], Archana Yadav[3], Tatiana Saraiva[4,5], Luke A. Hammond[2,6], Christoph Wirblich[7], Bosiljka Tasic[1], Vilas Menon[3], Joaquim Alves da Silva[4,8], and Rui M. Costa[1,2,9*]

1 Allen Institute, Seattle, WA 98109, USA
2 Zuckerman Mind Brain Behavior Institute, Columbia University, New York, NY 10027, USA
3 Center for Translational and Computational Neuroimmunology, Department of Neurology Columbia University Irving Medical Center, New York, NY 10032, USA
4 Champalimaud Research, Champalimaud Foundation, Lisbon 1400-038, Portugal
5 Department of Neurology, University Hospital of Würzburg, Würzburg 97080, Germany
6 Department of Neurology, The Ohio State University, Columbus, OH 43210, USA
7 Department of Microbiology and Immunology, Sidney Kimmel Medical College, Thomas Jefferson University, Philadelphia, PA 19107, USA
8 NOVA Medical School, Universidade Nova de Lisboa, Lisbon 1169-056, Portugal
9 Aligning Science Across Parkinson's (ASAP) Collaborative Research Network, Chevy Chase, MD, 20815
*Correspondence: akira.fushiki@alleninstitute.org (AF) and rui.costa@alleninstitute.org (RMC)

Abstract

In Parkinson's disease (PD), dopaminergic neurons (DANs) in the midbrain gradually degenerate, with ventral substantia nigra pars compacta (SNc) DANs exhibiting greater vulnerability. However, it remains unclear whether specific molecular subtypes of ventral SNc DANs are more susceptible to degeneration in PD, and if they contribute to the early motor symptoms associated with the disease. We identified a subtype of *Sox6*+ DANs, *Anxa1*+, which are selectively lost earlier than other DANs, and with a time course that aligns with the development of motor symptoms in MitoPark mice. We generated a knock-in Cre mouse line for *Anxa1*+ DANs and showed differential anatomical inputs and outputs of this population. Further, we found that the inhibition of transmitter release in *Anxa1*+ neurons led to bradykinesia and tremor. Therefore, *Anxa1*+ is not only a biomarker of a selectively vulnerable subtype of DANs, but is also sufficient to drive early motor symptoms in Parkinson's disease.

Keywords

Parkinson's disease, dopamine, cell types, neurodegeneration, vulnerability, tremor, motor symptoms

Introduction

Parkinson's disease (PD) is a progressive neurological disorder that primarily affects movement. It develops gradually, sometimes starting with a barely noticeable tremor in one hand[1]. While tremors, rigidity and akinesia are well-known signs of PD, the most distinctive symptom is bradykinesia, characterized by the slowing of movements. The main pathological hallmark of PD is the loss of dopaminergic neurons (DANs) in the substantia nigra[2,3] and the progressive reduction of DANs worsens the motor symptoms over time.

DANs in the midbrain are heterogeneous and they differ in their cellular properties and functions[4,5]. This heterogeneity is evident across several dimensions, including their molecular profiles and connectivity[4,6]. Transcriptomic studies have revealed that populations of midbrain DANs can be differentiated by distinct gene expression profiles[4], a finding that extends beyond the conventional anatomical division of midbrain DANs into the substantia nigra pars compacta (SNc, A9) and the ventral tegmental area (VTA, A10). Recent findings have discovered that molecularly unique subtypes of DANs innervate different subregions of the striatum, suggesting a basis for the variety of behavioral responses linked to these distinct neural pathways[5,6]. In PD, the degeneration of DANs follows a stereotypical pattern where some populations of neurons are more vulnerable than others[7]. Within the SNc, there is a distinction between the ventral-tier and dorsal-tier DANs, where the ventral-tier neurons tend to degenerate first[7]. Other studies have focused on changes in gene expression associated with PD compared to healthy controls[8]. Transcriptomic analysis revealed significant upregulation of alpha-synuclein[9] and downregulation of parkin[10], which are critical to dopamine synthesis and degradation pathways, respectively. This distinct expression pattern suggests a disruption in the proteostasis network that could be pivotal in disease progression. Additionally, genes related to mitochondrial function showed decreased expression levels, consistent with the known impact of mitochondrial dysfunction in Parkinson's pathology[11,12]. This differential gene expression or susceptibility aligns with the recent discovery of the distinct axonal projection patterns identified in dopaminergic neuron subtypes[6]. These patterns determine specific neural circuits affected during disease progression, providing a mechanistic basis for the diverse behavioral changes observed. For instance, subtypes projecting to motor-related areas may influence movement deficits, while those targeting limbic regions might underlie emotional or cognitive disturbances, illustrating how circuit-specific vulnerability translates into varied clinical manifestations[4–6]. However, it is not completely understood if specific molecularly identifiable subtypes of DANs in the ventral SNc are especially vulnerable in PD, and if the loss of function of these early

70 vulnerable populations is just a biomarker of the disease or contributes to the early motor
71 symptoms associated with PD.
72 Here, we characterized the progression of behavioral symptoms and dopaminergic
73 degeneration in MitoPark mice, a well-established PD mouse model[13], which replicates key
74 aspects of the disease through the targeted deletion of the *Tfam* (mitochondrial transcription
75 factor A) gene in DANs using the Cre-LoxP system. We characterized their motor behaviors in
76 an open field with a motion sensor and identified bradykinesia and a tremor gradually emerging
77 as MitoPark mice showed progressive dopaminergic degeneration in the SNc. We then
78 performed single-nucleus RNA-sequencing (snRNA-seq) in MitoPark mice and matched
79 littermate controls at different ages to identify transcriptomic changes in vulnerable
80 dopaminergic populations, and correlated the susceptibility of different cell types to
81 degeneration with the emergence of behavioral phenotypes. We identified specific dopaminergic
82 cell types, highly ventrally localized *Sox6+* neurons, whose loss was timeline-wise correlated
83 with the onset of motor symptoms. Further, we found that a subpopulation of the *Sox6+* neurons
84 – the *Anxa1+* subset is more vulnerable than other *Sox6+* populations. We next created an
85 Anxa1-Cre knock-in mouse to study the circuit architecture and function of this dopaminergic
86 neuron subtype. We characterized the anatomical inputs and outputs and observed a specific
87 pattern of strong projections of *Anxa1+* neurons to the dorsal striatum, not seen in other DAN
88 populations, and observed that this subtype also receives different inputs than others. Finally,
89 we showed that specific functional impairment of *Anxa1+* neurons is sufficient to induce
90 slowness of movements and motor tremors, corresponding to the early PD-like symptoms.
91 These results suggest that a specific vulnerable subtype of DANs is responsible for a range of
92 early motor symptoms of PD, potentially highlighting the role of different dopaminergic neurons
93 subtypes in the progression of the disease.
94
95 **Results**
96 **Progressive development of PD-like motor deficits in MitoPark mice**
97 The MitoPark mouse (genotype: *Tfam-loxP/loxP*, *+/DAT-cre*) is a transgenic model of
98 Parkinson's disease (PD) where the mitochondrial transcription factor A (*Tfam*) is removed
99 selectively in dopaminergic neurons (DANs)[13]. Loss of *Tfam* in DANs leads to a progressive
100 degeneration of these neurons and the manifestation of motor symptoms that are PD-like[13,14].
101 We characterized spontaneous movement of MitoPark mice between 8 and 24 weeks of
102 age in a square open field without any external cues or reward. These mice showed gradual
103 development of locomotor deficits post-natal with decreased average speed (bradykinesia),

104 increased immobility time and increased number of stops (akinesia) (**Fig.1A-1D**). These effects
105 were independent of environmental novelty, as similar differences were observed in both novel
106 and habituated environments (**Fig.1B-1D and Extended Data Fig.1A and 1B**). We also
107 performed a cylinder task to observe rearing behavior, which is more effortful and therefore
108 more likely to be affected in PD, where there is a tendency towards less vigorous movements.
109 We indeed confirmed a significant reduction in the number of rears in the older MitoPark mice
110 (**Fig.1E**). Given that typical PD has other motor symptoms, such as tremor in addition to
111 bradykinesia and akinesia, we used a wireless motion sensor to detect subtle motor changes
112 that are not easily observable by video-characterization. The sensor measures tri-axial
113 acceleration with high resolution and allows for the continuous monitoring of movement with
114 high frequency (200Hz)[15], which could enable us to detect tremors that are usually poorly
115 documented in genetically engineered rodent models of PD[16]. Given that tremor is defined as an
116 involuntary rhythmic and oscillatory movement of a body part[17], we explored spectral analysis of
117 accelerometer data to quantify the potential emergence of abnormal oscillations with the
118 progressive degeneration of DANs. Interestingly, we observed a specific oscillation within the
119 12-18 Hz frequency band that emerged in MitoPark mice at 16 weeks which gradually
120 intensified with age (**Fig.1F-1I and Extended Data Fig.1C and 1D**). Notably, this oscillation
121 was present even when the mice were immobile (**Fig.1G and 1I**).
122 We next examined whether depletion of SNc DANs would be sufficient to lead to the
123 development of PD-like symptoms similar to those observed in MitoPark mice. We therefore
124 genetically ablated the neurons in the SNc of DAT-Cre mice by bilateral stereotactic injection of
125 an adeno-associated virus (AAV) to express a Cre-dependent apoptotic gene Caspase-3 (AAV-
126 Ef1a-FLEX-taCasp3)[18] in the SNc of DAT-Cre mice. Selective losses of the SNc DANs and their
127 projections were observed after 4 weeks of viral expression (**Fig.1J**). We evaluated mice
128 behavior in the open field, and found that the depletion of SNc DANs reproduced the PD-like
129 phenotype observed in the 24 weeks of MitoPark mice (**Fig.1A-1D, 1K, 1M and Extended Data**
130 **Fig.1E–1H**). We also observed a marked reduction in rearing behavior in the animals with
131 ablation of SNc DANs (**Fig.1L and 1N**). Furthermore, we also replicated the emergence of the
132 tremor as observed in MitoPark mice (**Fig.1O and 1P**). These results suggest that the neuronal
133 loss in the SNc is sufficient to produce the bradykinesia, akinesia, and tremor observed in the
134 MitoPark mice.
135
136 **Progressive loss of dopamine neurons in the ventral midbrain in MitoPark mice**

137 To determine whether the mitochondrial *Tfam* deficit leads to changes in the number of midbrain
138 DANs, we surveyed *Th* expression in MitoPark mice and monitored changes in *Th*+ cells in the
139 SNc of MitoPark mice at 8, 16 and 24 weeks (**Fig.2A and 2B)**. We also examined *Th*+ axonal
140 projections from the SNc of MitoPark mice to striatum and performed brain reconstruction.
141 Given that the current Allen Common Coordinate Framework (Allen CCF) does not have
142 anatomical subdivisions of the striatum[19], we created an updated map based on cortical
143 projections[20] and applied the imaging analysis pipeline BrainJ as previously described[21]
144 (**Extended Data Fig.2**). This updated atlas allowed us to quantitatively analyze the density of
145 projections neurons in subregions of the striatum and visualize the prominent loss of *Th*+ axonal
146 projections in MitoPark mice (**Fig.2C and Extended Data Fig.2C)**. We observed no observable
147 differences in the projections from SNc DANs to the striatum at 8 weeks in MitoPark mice.
148 However, by 16 weeks, their projections were significantly reduced compared to age-matched
149 controls, especially for those targeting the dorsal striatum. By 24 weeks, the projections were
150 largely depleted. (**Fig.2A and 2C)**. Comparable progression has been reported in MCI
151 (mitochondrial complex I)-Park mice in a previous study[12].
152 We also employed single-nucleus RNA sequencing (snRNA-seq) of the ventral midbrain
153 of MitoPark mice, their littermate controls (genotype: *Tfam-loxP/loxP*, +/+ or *Tfam-loxP/*+, +/+)
154 and C57BL/6 (B6) mice at 8, 16, and 24 weeks of age (8 mice in each group; 4 males and 4
155 females). We used a previously described experimental approach to isolate nuclei and profile
156 their transcriptomes from mice[22] (**Fig.2D and Extended Data Fig.3A**, see "Methods" section).
157 We obtained a total of 293,435 nuclei, of which 93,703 were from MitoPark mice, 100,266 were
158 from their littermate controls and 99,466 were from B6 mice. We mapped cell annotations to our
159 data with the Allen Brain Cell (ABC) Atlas using their MapMyCells tool[23] (**Fig.2E and Extended**
160 **Data Fig.3B**). Dopaminergic nuclei were identified as the subclass annotation of
161 215_SNc_VTA_RAmb_Foxa1_Dopa at the ABC Atlas, within the class annotation of
162 21_MB_Dopa (**Extended Data Fig.3B**). The dopaminergic population was also clearly
163 distinguished by expression of the canonical marker gene, *Th* (**Fig.2F**). Using *Rbfox3* to mark
164 neuronal cells, we identified other neuronal cell types such as excitatory (*Slc17a6*) and inhibitory
165 (*Slc32a1*) cell types (**Fig.2F and Extended Data Fig.3C**). Oligodendrocytes were characterized
166 by the expression of *Mog*, while Oligodendrocyte precursor cells (OPCs) expressed high levels
167 of *Pdgfra*. Microglia were characterized by *Ptprc* expression, while astrocytes and endothelial
168 cells were marked by specific expression of *Gja1* and *Nostrin*, respectively (**Extended Data**
169 **Fig.3C**). Consistent with our histological findings, we observed a significant decrease in the
170 number of DANs in MitoPark mice between 8 weeks and 24 weeks (**Extended Data Fig.4A**). To

171 address whether cell types are enriched or depleted in MitoPark mice, we compared the
172 proportions of all cell-types across the ventral midbrain at each stage. We found that the
173 dopaminergic populations significantly decreased with age compared with other cell types
174 (**Extended Data Fig.4B**). We also performed mixed-effects modeling (MASC)[24] that accounts
175 for technical and biological confounders to identify cellular populations associated with the
176 disease models (**Fig.2G-2I and Extended Data Fig.4C-4E**). MitoPak mice had a significant
177 reduction of DANs at 16 and 24 weeks relative to their littermate controls, while the other cell-
178 types were stable (**Fig.2G, 2H, Extended Data Fig.4C and 4D**). A similar reduction of DANs
179 was also observed between 8 and 16 weeks in the same genotype (**Fig.2I and Extended Data**
180 **Fig.4E**). Together, these data demonstrate that *Tfam* depletion in MitoPark mice induces robust
181 and selective dopaminergic degeneration without altering the number of other neighboring cell
182 types (**Fig.2G-2I and Extended Data Fig.4B-4E**).
183
184 **Vulnerability of *Sox6*+ population during the progression of PD-like phenotypes**
185 We next aimed to identify changes within specific subtypes of DANs during the progression of
186 neurodegeneration. We isolated 18,611 DANs from nuclei of the ventral midbrain, and snRNA-
187 seq data was processed to identify distinct groups representing unique neuronal subtypes
188 (**Fig.3A, Extended Data Fig.5A and 5B**). We identified 8 DAN subtypes and confirmed the
189 expression of well-known subtype markers *Sox6*, *Slc17a6, and Calb1*[4] (**Fig.3B**). Each group
190 was segregated by distinct genetic markers, which included known dopaminergic neuron
191 subtype-specific genes (**Extended Data Fig.5C and 6A-6C**). To determine which neuronal
192 subtypes were most affected as neurodegeneration progressed, we analyzed the cell
193 composition within each identified group from MitoPark mice and their age-matched controls.
194 Comparative analysis showed significant changes in the composition of dopaminergic neuronal
195 subtypes (**Fig.3C**). Notably, the proportion of *Sox6*+ neurons was markedly reduced in MitoPark
196 mice, whereas the proportion of other neuron cell types such as *Megf11*+ or *Synpr*+ remained
197 'stable' throughout the degeneration process. As the overall number of dopamine neurons
198 decreases in MitoPark mice, the proportion of these 'stable' neurons increased, suggesting they
199 are more resilient compared to other dopamine subtypes that are more susceptible to
200 degeneration (**Fig.3C**). These neurons are mostly *Vglut2*+ (*Slc17a6*) (**Fig.3A and 3B**), which
201 has previously been reported to play a potential neuroprotective role in the survival of DANs in
202 PD model animals[25,26]. Additionally, there are dopamine neuron subtypes that undergo uniform
203 degeneration over time (*Plekhg1*+, *Cck*+, *Sema5b*+, *Etv1*+, *Lypd1*+) (**Fig.3C**). Using the MASC
204 approach, we further analyzed the differential proportion of different cell-types or states across

205 different groups (**Fig.3D-3F**) while adjusting for age, sex, and batch as covariates. The *Sox6+*
206 population showed a significant decrease in the odds ratio in MitoPark mice compared to their
207 littermate controls, especially at 16 or 24 weeks (**Fig.3D and 3E**), and it was not due to age-
208 related effects alone (**Extended Data Fig.6D-6G**). We also conducted the test across different
209 ages within the same genotype to assess developmental changes in cell population dynamics
210 (**Fig.3F**). The odds ratio of *Sox6+* population still declined, suggesting that this subtype exhibits
211 greater vulnerability than other DANs in PD, consistent with findings from human PD
212 transcriptomic studies[8].
213
214 **A subset of *Sox6+* DANs are more vulnerable in MitoPark mice**
215 *Sox6* is involved in the development and differentiation of DANs, particularly in the ventral
216 midbrain DANs[27–29]. The *Sox6+* supertype (ID: 0882 in 215_SNc_VTA_RAmb_Foxa1_Dopa)
217 can be further subdivided according to their anatomical location, distinct molecular signatures,
218 and functional properties[4]. To explore the diversity of *Sox6+* neurons, we conducted
219 transcriptomic analysis of the subtypes and performed the cluster annotation based on the ABC
220 atlas[23]. We found 43 clusters (ID: 3837-3879) under the supertype (ID: 0880-0887) annotation,
221 of which, the *Sox6+* supertype can be divided into 7 subsets (ID: 3853-3859) (**Extended Data**
222 **Fig.5A**). We quantified the proportions of *Sox6+* dopaminergic subtypes in MitoPark and control
223 animals. Two subsets, *Anxa1+* (ID: 3857) and *Arpp21+* (ID: 3859), showed statistically
224 significant reductions compared to controls (two-way ANOVA followed by Tukey's HSD).
225 *Anxa1+* was significantly reduced across age, whereas *Arpp21+* reached significance only at 24
226 weeks (**Fig.4A**). Although other *Sox6+* subsets showed a tendency toward reduced proportions
227 in MitoPark animals, this pattern prompted the use of a complementary differential abundance
228 analysis. We therefore performed an additional differential abundance analysis using Milo, a
229 method that offers a structured approach to exploring variations in cell compositions across
230 diverse experimental conditions[30] (**Fig.4B-4J and Extended Data Fig.7A-7I**). Milo analysis
231 confirmed a significant depletion of *Sox6+* population in MitoPark mice at 16 and 24 weeks
232 compared to their littermate controls, consistent with previous analyses (**Fig.3C-3F and**
233 **Extended Data Fig.7A-7I**). Following cluster annotation, most *Sox6+* subsets exhibited
234 pronounced reductions in gene expression at 16 and 24 weeks (log fold change < −3 at 16
235 weeks and < −5 at 24 weeks; **Fig.4E, 4F, 4H and 4I**). Additionally, comparison between 8 and
236 16 weeks in MitoPark animals revealed two subsets (*Grin2c+* (ID: 3854) and *Anxa1+* (ID:
237 3857)) with robust gene expression decreases (log fold change < −2; **Fig.4D, 4G, 4J, and**
238 **Extended Data Fig.7J-7L**). An additional analysis using a linear mixed-effects model (LMM)[31],

239 followed by Tukey's post hoc comparisons, showed that the 3857_Anxa1 cluster consistently
240 exhibited the strongest and most statistically significant age-by-genotype interaction, and further
241 indicated that this cluster is already slightly affected at 8 weeks (MitoPark vs. Control; 8 weeks:
242 2.37E-03, 16 weeks: 3.34E-06, 24 weeks: 1.41E-04)[31]. We also compared DAT expression
243 across *Sox6+* dopaminergic subtypes and found no significant differences, indicating that
244 selective vulnerability is unlikely to be driven by DAT levels (**Extended Data Fig.7M**). To verify
245 the transcriptional reduction of DAN subsets in the SNc of MitoPark mice, we conducted
246 immunostaining with an antibody targeting *Aldh1a1*, a well-established marker for ventral
247 DANs[4,5] (**Fig.4K**). *Aldh1a1+* neurons constitute a relatively large neuronal subset and are
248 recognized as selectively vulnerable in PD, encompassing the *Anxa1+* population in the ventral
249 SNc[5,32–34]. We found a remarkable loss of *Aldh1a1+* DANs in MitoPark mice at 16 weeks,
250 particularly in the rostral-ventral region (**Fig.4K**). These results demonstrate that *Sox6+* DANs
251 exhibited differential susceptibility, with *Anxa1+* DANs emerging as one of the earliest
252 populations to show vulnerability relative to other DANs.
253
254 **Whole-brain efferent and afferent connectivity of *Anxa1+* DANs**
255 The results above indicate a subset of *Sox6+* DANs, the *Anxa1+* neurons, is more vulnerable
256 than others. However, it remains unclear whether loss of these neurons is an early biomarker of
257 disease, or are actually driving early symptoms in PD. To address this, we generated an Anxa1-
258 Cre knock-in mouse line (see 'Method' section), with Cre recombinase under transcriptional
259 control of an Anxa1-specific promoter and characterized its expression using GFP to visualize
260 cell bodies and axon projections to output structures. To achieve this, we injected Cre-
261 dependent AAV-GFP into the SNc of Anxa1-Cre mice and counted the number of *Th+* cells with
262 *Calb1* antibody, which labels the dorsal dopaminergic populations in the SNc (**Fig.5A and 5B**).
263 In all mice, we observed robust co-localization of GFP with *Th+* cells but not *Calb1+* cells,
264 suggesting that most of the GFP+ cells in the SNc are ventral specific DANs (**Fig.5A and 5B**).
265 We then examined GFP+ axonal projections from the SNc of all DANs or *Anxa1+* DANs and
266 performed whole brain reconstruction using BrainJ (**Fig.5C and 5D)**. The quantitative analysis
267 revealed prominent axonal projections of *Anxa1+* DANs to the dorsal striatum (**Fig.5D**). We also
268 created a DAT-Flp knock-in mouse line[35] (**Extended Data Fig.9A;** see 'Method' section) and
269 compared the axonal projections of SNc *Anxa1+* DANs with other DANs subtypes such as
270 *Vglut2+* or *Calb1+* (**Extended Data Fig.9B**). As shown previously[6], these subsets have distinct
271 axonal projections to the striatum; *Vglut2+* DANs project to the dorsolateral and tail striatum,
272 while *Calb1+* DANs project to the ventral striatum (**Extended Data Fig.9B**). We also

273 quantitatively analyzed SNc *Vglut2*+ and *Calb1*+ DAN axonal projections throughout the whole
274 brain, which make specific projections to many different regions. The fact that different
275 populations of DANs have such distinctive projections opens the possibility that different
276 populations modulate different behaviors or behavioral parameters[5] (**Extended Data Fig.9C)**.
277 To identify the afferent inputs onto *Anxa1*+ dopaminergic neuronal subtypes and how
278 these inputs differ from other DAN subtypes, we used CVS-N2c rabies tracing, a strain with
279 enhanced transsynaptic labeling[36], with DAT-Cre+, Anxa1-Cre+ (and also DAT-Flp+;Anxa1-
280 Cre+), DAT-Flp+;Vglut2-Cre+ and DAT-Flp+;Calb1-Cre+ mice. We first examined the inputs to
281 all DANs in the SNc by injecting two Cre-dependent helper viruses (TVA and N2cG) to express
282 the avian receptor (TVA protein) and the rabies glycoprotein G (N2cG) unilaterally into the SNc
283 of DAT-Cre+ mice. Two weeks later, CVS rabies virus (CVS-tdTomato) was injected into the
284 same site (**Extended Data Fig.10A;** see "Methods" section**)**. We observed tdTomato-labeled
285 neurons in more brain regions than previous studies[37,38], especially detected much more inputs
286 for cortical regions, likely attributed to the higher transsynaptic property of the N2C strain. These
287 labeled neurons, primarily restricted ipsilateral to the injection site, represent monosynaptic
288 afferent inputs to the SNc DANs (**Fig.5F, 5G and Extended Data Fig.10B, 10C**). The same
289 viral injection strategy was also used using Anxa1-Cre+ (and DAT-Flp+;Anxa1-Cre+), DAT-
290 Flp+;Vglut2-Cre+, and DAT-Flp+;Calb1-Cre+ mice, which also labeled an abundant number of
291 tdTomato+ neurons in various parts of brain regions (**Fig.5E, 5H, 5I and Extended Data**
292 **Fig.9D-9G**). The dopaminergic neuron subtypes exhibit modest differences in their ipsilateral
293 inputs, particularly with respect to inputs from cortical regions. For example, while *Anxa1*+ DANs
294 receive strong inputs from the motor cortex, this subtype does not receive significant inputs from
295 the somatosensory, prelimbic, or orbital cortex. In contrast, *Vglut2*+ DANs receive minimal
296 inputs from the ventral regions of the anterior cingulate and retrosplenial cortices compared to
297 other dopamine subtypes. In most other cases, however, *Anxa1*+ DANs receive similar inputs to
298 the other dopaminergic subtypes, suggesting a far more shared organization of inputs into SNc
299 dopaminergic circuits than their outputs (**Fig.5E-5I and Extended Data Fig.9D-9G**).
300
301 **Inhibition of *Anxa1*+ DANs is sufficient to cause early PD-like motor deficits**
302 The activity of *Anxa1*+ neurons has been shown to correlate with movement acceleration[5]. To
303 determine whether the loss of *Anxa1*+ neurons represents an early biomarker of disease or
304 contributes causally to early PD symptoms, we selectively silenced synaptic release from
305 *Anxa1*+ dopaminergic neurons using an AAV expressing tetanus toxin[39] (AAV-FLEX-TeLC-
306 EYFP; **Fig.6A**). We found that silencing of *Anxa1*+ neurons caused a reduction in locomotor

speed, suggesting it is sufficient to cause bradykinesia. However, it did not affect immobility time or number of stops, suggesting that it was not sufficient to cause akinesia. (**Fig.6B-6D**). In a cylinder task, we observed the significant drops in the number of rears, suggesting that *Anxa1+* dopaminergic neuron activity is important for effortful movements (**Fig.6C)**. We then performed spectral analysis on mice depleted of *Anxa1+* SNc dopaminergic neurons and found a slight shift in the frequency of tremor, resembling the phenotype of MitoPark mice at 16 weeks (**Fig.6E**).

Learning is also known to be affected early in PD and in MitoPark animals[40,41]. Given the early vulnerability of *Anxa1+* neurons, we wanted to determine whether their loss is sufficient to cause learning deficits, or if other neuronal populations are responsible. We used a Pavlovian conditioning task in which mice learned to lick for a reward when presented with a light cue. In this paradigm, a visual cue (CS+; LED stimulus) signaled the availability of a sucrose reward, delivered at random intervals, whereas an auditory cue (CS–; sound) was never paired with reward (**Extended Data Fig.11A**). Thus, CS+ presentations should elicit increased reward expectation, reflected by elevated licking despite the unpredictability of cue timing. Across conditioning days, control mice showed a progressive increase in licking following CS+ presentation, indicating successful learning of the cue–reward association. In contrast, Anxa1-TeLC mice displayed markedly reduced licking responses (**Extended Data Fig.11B**). To determine whether these effects were due to impairment in licking, we also analyzed poke events (**Extended Data Fig.11C**). Control mice showed prompt, cue-triggered poking beginning on Day 2, whereas Anxa1-TeLC mice exhibited random, non–cue-directed poking. Total lick counts across each session did not differ between groups, and total poke counts showed a similar pattern except on Day 1 (**Extended Data Fig.11D and 11F**). However, both the first-lick and first-poke latencies were significantly prolonged in Anxa1-TeLC mice, although these delays gradually decreased over days (**Extended Data Fig.11E and 11G**).

Taken together, these data show that inhibition of *Anxa1+* DANs is sufficient to induce early PD-like features such as reduced movement speed, diminished movement vigor, tremor, and learning deficits, yet not sufficient to produce akinesia.

Discussion

The data presented in this study revealed that a subtype of dopaminergic neurons (DANs) is selectively vulnerable in a mouse model of Parkinson's disease (PD) and that its loss is sufficient to drive PD-like motor symptoms that are observed early in the disease. We conducted a detailed longitudinal analysis of the behavioral changes exhibited by MitoPark

341 mice, a well-established PD model[13]. We identified progressive changes in bradykinesia,
342 akinesia, and tremor. Concomitantly, these mice demonstrated a progressive degeneration of
343 DANs in the midbrain, specifically within the substantia nigra pars compacta (SNc). These
344 phenotypes observed in late-stage MitoPark mice were replicated by ablating DANs in the SNc.
345 Additionally, we performed a comprehensive characterization of the molecular profiles of
346 midbrain neurons as the disease progressed, and uncovered selective vulnerability in the *Sox6+*
347 DANs, and in particular in the *Anxa1+* subtype. Finally, we observed that silencing this
348 dopamine subtype was sufficient to produce bradykinesia and tremor of the magnitude
349 observed early in the progression of the degeneration, but not akinesia. This reveals that the
350 loss of these vulnerable neurons is not only a biomarker of early disease, it also drives the early
351 motor symptoms observed early in the disease.
352 Our behavioral analysis rigorously mapped the progression of motor symptoms in
353 MitoPark mice revealing early symptoms that were not previously reported. Furthermore, it
354 revealed a previous unobserved phenotype associated with dopamine loss. By using a motion
355 sensor in an open field behavioral assay, we have enhanced our capability to detect more
356 subtle motor phenotypes that are not detected using conventional video-based characterization
357 methods. This approach led us to identify tremors in MitoPark mice, which developed
358 incrementally with the progressive degeneration of DANs in the brain. Furthermore, specific
359 ablation and silencing of SNc DANs and the *Anxa1+* subtype revealed their important role in this
360 tremor phenotype. Although the significance of the oscillation frequency we observed remains
361 under investigation, the ~10 Hz signal in control mice most likely reflects a physiological tremor
362 linked to postural stabilization and the natural resonance of the sensorimotor system. In
363 contrast, the tremor seen in MitoPark and dopamine-lesioned mice even during rest suggests
364 the emergence of a central, PD-related tremor or increased rigidity that shifts the mechanical
365 tremor frequency. Notably, the tremor frequencies in MitoPark mice do not fall within the typical
366 4-6 Hz range observed in PD patients[42]; however, species-specific differences in tremor
367 frequency are well documented, as illustrated by the harmaline model of essential tremor, which
368 produces oscillations of 8–10 Hz in monkeys, 10–12 Hz in rats, and 11–14 Hz in mice[43,44].
369 Considering that there are several types of tremors observed in humans and the extent to which
370 these tremors resemble those seen in human diseases has not yet been fully established, a
371 more comprehensive characterization is imperative. Another key discrepancy between human
372 PD and PD mouse models is that, in early-stage patients, motor symptoms such as resting
373 tremor and bradykinesia typically emerge asymmetrically due to greater dopaminergic neuron
374 loss in one hemisphere, producing a unilateral and focal onset that later becomes bilateral[45]. In

375 contrast, PD mouse models generally exhibit more symmetric dopaminergic degeneration,
376 resulting in bilateral, whole-body tremors and limiting the detection of focal symptom onset. The
377 human and mouse musculoskeletal systems also differ substantially, which may contribute to
378 the distinct tremor frequencies observed and reflect species-specific postural demands. This
379 interpretation is supported by a recent study that employed similar inertial sensors in patients
380 with PD[46]. These differences likely arise from both species-specific pathological features and
381 the whole-body nature of our behavioral assessments.
382 In previous studies, *Aldh1a1+* DANs have been shown to be selectively vulnerable in
383 PD[32]. Their properties including connectivity and firing patterns have been extensively
384 characterized, and these works have highlighted their relevance to motor control and PD
385 pathophysiology[32–34]. It has also been shown that *Aldh1a1+* neurons comprise distinct genetic
386 and functional subsets[5], which motivated us to perform independent molecular profiling. We
387 performed an extensive longitudinal molecular profiling of the cell types in the ventral midbrain
388 as the symptoms progressed in MitoPark mice, utilizing a newly developed atlas, the Allen Brain
389 Cell (ABC) Atlas, for annotation[23]. This detailed examination identified a vulnerable population of
390 DANs, *Sox6+*, the characteristics of which align closely with those identified in previous human
391 and mouse studies[8]. In contrast, other subtypes, such as *Megf11+* (ID: 0880), and *Synpr+* (ID:
392 0887) displayed resilience to degeneration. We identified several additional subtypes of *Sox6+*
393 DANs, with different vulnerability. *Anxa1+* (ID: 3857) neurons showed the earliest significant
394 decrease compared to the littermate controls, but *Arpp21+* (ID: 3859) also showed vulnerability
395 in late stages compared to other subtypes of *Sox6+* neurons. This early vulnerability was also
396 observed in other mouse models and in humans in an accompanying study[47–49]. This variance in
397 vulnerability and resilience indicates that the degeneration of DANs occurs at different rates in
398 different types, and that the molecular composition of these subtypes may underly the
399 mechanisms for vulnerability and resilience. Consequently, a deeper understanding of the
400 molecular processes driving the degeneration and resilience of these various DAN subtypes is
401 critical for understanding the progression of the disease, and could be harnessed for the
402 development of biomarkers to monitor progression and eventually the response to disease
403 modifying therapies.
404 We also characterized with unprecedented depth the afferent and efferent connectivity of
405 three distinct subtypes of DANs in the SNc, roughly representing lateral, dorsal, and ventral SNc
406 DANs, identified by the expression of genes *Vglut2+*, *Calb1+*, and *Anxa1+* respectively.
407 Consistent with previous reports, these subtypes display distinct projection patterns within the
408 striatum, occupying specific subregions; for example, *Anxa1+* neurons preferentially project to

409 the dorsal striatum, a region critical for motor control[6]. This supports the conclusion that these
410 subtypes display divergent behaviors in motor control and reward processing[5]. However, our
411 results also reveal that, despite their distinct projection patterns, these subtypes receive
412 largely similar inputs across the brain, with some exceptions in cortical regions. This aligns with
413 the idea that many dopamine neurons within a given region exhibit similar activity patterns, and
414 suggests that their differential vulnerability is unlikely to be driven by differences in synaptic
415 input. Still, several possibilities remain. One is that even subtle in input differences (for example,
416 cortical regions in this case) may still have functional consequences. Alternatively, spatially
417 distinct DAN subpopulations may receive inputs from different neuron groups within the same
418 area, leading to distinct functions. Finally, SNc neurons may share broadly similar computational
419 properties but display subtle differences in their response profiles. Their functional divergence
420 may ultimately arise from how their projections interface with specific downstream cell types -
421 for example, through the receptors expressed by their targets. A further layer of complexity
422 emerges from the recurrent loop between the striatum and SNc: SNc dopaminergic neurons
423 receive substantial inhibitory input from striatal medium spiny neurons while simultaneously
424 projecting back to them[50,51]. The distinct projection profiles of dopaminergic neuron subtypes
425 may therefore shape striatal dynamics in unique ways, with inhibitory feedback mechanisms
426 subsequently fine-tuning dopaminergic signaling during diverse behavioral and learning
427 processes. Additionally, a more detailed classification of the inputs and projections of each DAN
428 subtype would be necessary to define specific input–output cell types, rather than the broader
429 regional categories used here, as has been demonstrated in studies of fruit flies at the single-
430 cell level[52]. For example, one of the major sources of input, the midbrain reticular nucleus
431 (MRN), contains a heterogeneous mix of cell types, including glutamatergic and GABAergic
432 neurons[53]. Unfortunately, our current methods do not allow us to determine which specific cell
433 types contribute to the observed inputs. This granular approach may reveal intricate
434 neurobiological dynamics obscured when broader classifications are used.
435 Finally, a recent study showed that *Anxa1+* neurons constitute a genetically distinct
436 subset within the *Aldh1a1+* population and are functionally different from other dopaminergic
437 subtypes, as demonstrated using their own transgenic line[5]. In parallel, we generated our own
438 transgenic mouse line to manipulate these neurons with similar specificity. Although targeted
439 manipulation of *Anxa1+* neurons led to significant bradykinesia and tremor similar to those
440 observed in the early stages of disease in MitoPark mice, it did not affect immobile time or
441 akinesia. These discrepancies might be explained by a dosage effect (i.e. akinesia requires the
442 loss of more dopamine neurons than bradykinesia), or most likely by the involvement of other

443 dopaminergic neuron subtypes that contribute to phenotypes emerging at later stages. For
444 example, degeneration of *AGTR1+* or *Calb1+* neurons may also contribute to motor symptoms
445 in the PD phenotype[8,54]. However, the motor deficits differ from those reported during *Anxa1+*
446 neuron inhibition[48]. Thus, our study does not argue that *Anxa1+* neurons are the sole
447 contributors to motor impairment. Rather, we show that their early loss is sufficient to generate
448 motor deficits resembling those seen in early PD. In addition to the motor symptoms, we also
449 found that inhibition of *Anxa1+* neurons produced a learning deficit. Given that cognitive
450 dysfunction has been reported to precede motor symptoms in MitoPark mice[41], these results
451 suggest that *Anxa1+* neurons may also contribute to early non-motor symptoms as well.
452 However, given that other dopaminergic subtypes are also affected such as *Arhgap28+*
453 neurons, our data do not exclude the possibility that additional cell types within the same group
454 may play a role in learning. Further investigation will be important, particularly in relation to other
455 early PD-associated features such as sleep behavior disturbances or constipation. The
456 possibility of homeostatic compensation within DAN neural networks, with different neurons
457 stepping in to sustain the functionality of behaviors affected by the loss of others, should also be
458 discussed. We observed considerable overlap in the brain regions providing afferent
459 connectivity to each dopamine subtype and this observation could be critical to understand the
460 adaptability of these circuits. A critical approach to further unravel these complexities of
461 adaptation as disease develops would involve recording whole-brain activity in PD model mice.
462 Gaining a deeper understanding of the resilience and adaptability of neural circuits surrounding
463 dopaminergic neurons will enhance our grasp of Parkinson's disease and potentially foster
464 innovative therapeutic strategies in the future.

465 **Materials and Methods**

466 **Contact for reagents and resource sharing**

467 All reagents and materials used in this study are listed in the Key Resources Table (DOI:
468 10.5281/zenodo.18273548). For additional information or requests, please contact the Lead
469 Contact, Rui M. Costa (rui.costa@alleninstitute.org).

470

471 **Mouse breeding and husbandry**

472 All experimental protocols were performed according to National Institutes of Health (NIH)
473 guidelines and in compliance with the regulations of the Institutional Animal Care and Use
474 Committee at Columbia University. All experimental animals were 2 to 6 month-old mice housed
475 on a 12 hr light/dark cycle with unrestricted access to food and water. Mice used for behavioral
476 experiments were individually housed. The strain and lines used were: C57BL6/J (Jackson
477 Laboratories, 000664), MitoPark mouse[13], DAT-Cre mouse (Jackson Laboratories, 006660),
478 VGlut2-Cre mouse (Jackson Laboratories, 028863), and Calb1-IRES2-Cre mouse (Jackson
479 Laboratories, 028532). Anxa1-Cre (Jackson Laboratories, 040185) and DAT-Flp (Jackson
480 Laboratories, 040184) mouse lines were developed and utilized in our lab (details are provided
481 below)[35]. MitoPark mice (*DAT-Cre*$^{+/-}$*;Tfam*$^{loxP/loxP}$) were obtained by crossing *DAT-Cre*$^{+/-}$*; Tfam*$^{loxP/+}$
482 mice with *Tfam*$^{loxP/loxP}$ mice to selectively knockout *Tfam* in dopaminergic neurons.

483

484 **Generation of transgenic mice (Anxa1-Cre and DAT-Flp)**

485 Anxa1-Cre and DAT-Flp knock-in mice were generated by Cyagen (Santa Clara, CA) using
486 CRISPR/Cas9. To generate Anxa1-Cre mice, one cell mouse embryos were microinjected with
487 Cas9 protein, a gRNA (5' GACATCCCAACTATTCTGCA-AGG 3') targeting exon 13 in the vicinity
488 of the stop codon, and a repair template comprised of homology arms and a 'P2A-Cre-rBG pA'
489 cassette. Homology arms were generated by PCR from BAC clones RP23-53N8 and RP23-
490 149B23 as template. Similarly, to generate DAT-Flp mice, a gRNA (5'
491 CCAACAGCCAATGGCGCAGC-TGG 3') targeting exon 15, and a template with a '2A-FlpO-rBG
492 pA' cassette were used[35]. Homology arms were PCR amplified from BAC clones RP23-150M11
493 and RP23-34F24. Two silent mutations, aa 613L (CTG to TTA), and aa 614R (CGC to AGG) were
494 introduced to prevent re-cleavage by Cas9 after homology-directed repair.

495

496 **Nuclear suspension, FACS and Single-nucleus RNAseq**

497 We used procedures as previously described[55,56]. Briefly, MitoPark mice and their littermate
498 controls (P56~62 for 8 weeks, P112~118 for 16 weeks and P168~174 for 24 weeks; 4 female and

499 4 male at each time point) were anaesthetized with isoflurane and perfused with cold artificial
500 cerebrospinal fluid (ACSF) containing N-methyl-d-glucamine (NMDG; 92 mM), KCl (2.5 mM),
501 NaH2PO4 (1.2 mM), NaHCO3 (30 mM), HEPES (20 mM), D-Glucose (25 mM), Sodium L-
502 ascorbate (5 mM), Sodium pyruvate (3 mM), MgSO4 (10mM), CaCl2 (0.5 mM), bubbled with
503 carbogen gas (95% O2 and 5% CO2) at a pH of 7.2–7.4. The brain was sectioned at 400um using
504 a vibratome (VT1200S, Leica Microsystems) on ice, and the ventral midbrain (SNc and VTA) were
505 microdissected from three consecutive sections (-2.48 to -3.88mm from Bregma; Franklin and
506 Paxinos, 2008). The tissues were transferred to microcentrifuge tubes, flash frozen in dry ice with
507 ethanol, and stored at -80C until later use. For nuclei isolation[22], frozen tissues were placed into
508 a homogenization buffer that consisted of 10mM Tris pH 8.0, 250mM Sucrose, 25mM KCl, 5mM
509 MgCl2, 0.1% Triton-X 100, 1X Protease inhibitor (Promega G6521), 0.5% RNasin Plus RNase
510 inhibitor (Promega N2615) and 0.1mM DTT (Promega P1171). Tissues were placed into a 2ml
511 dounce homogenizer (Sigma D8938) and homogenized using 10 strokes of the loose dounce
512 pestle followed by 10 strokes of the tight pestle to liberate nuclei. Homogenate was strained
513 through a 30µm cell strainer (Miltenyi Biotech 130-098-458) and centrifuged at 900xg for 10
514 minutes to pellet nuclei. Nuclei were then resuspended in blocking buffer containing 1X PBS
515 supplemented with 0.8% nuclease-free BSA (Sigma, OmniPur 2905) and 0.5% RNasin Plus
516 RNase inhibitor. Prior to fluorescence-activated nuclei sorting (FACS), DAPI (Sigma, D9542) was
517 applied to nuclei suspensions at a final concentration of 0.1µg/ml and nuclei suspensions were
518 filtered through a 30µm nylon mesh (Sysmex, 04-004-2326) to remove aggregates. FACS was
519 performed at the Zuckerman Institute Flow Cytometry platform using a MoFlo Astrios EQ
520 (Beckman Coulter) sorter. Single nuclei were captured by gating DAPI+ events, excluding debris
521 and doublets. Both cell suspension and collection chamber were kept at 4C during sorting. Sorted
522 nuclei were spun down immediately and barcoded using 10x Genomics Chromium Single Cell 3'
523 Reagent Kit v3 according to the manufacturer's protocol. Samples were processed and libraries
524 were prepared/sequenced by the Columbia JP Sulzberger Genome Center Single Cell Analysis
525 Core.
526
527 **RNAseq data processing and analysis**
528 Sequencing data were aligned and quantified using the Cell Ranger Single-Cell Software Suite
529 (v.6.1.2) with default parameters against the ENSEMBL GRCm38/mm10 reference genome[57].
530 The pre-filtered datasets were then imported into the R Seurat package for downstream analysis
531 (v5.0.2)[58]. We first removed low-quality cells (cell containing < 200 genes and genes expressed
532 in <3 cells of the data). After the filtering, contaminating ambient RNA reads were filtered by using

533 SoupX[59]. Doublets were predicted using the DoubletFinder R package[60], and were excluded for
534 downstream analysis. After quality control and cell filtering (1000<nFeature_RNA<7500;
535 nCount_RNA<40000; percent_mt<1, percent_ribo<1, percent_hemo<1), the datasets were
536 processed for identifying cell populations by Seurat pipeline. Briefly, pre-processed gene
537 expression matrices were normalized by the NormalizedData function. A total of 2,000 most
538 variable features were then selected with the FindVariableFeatures and scaled by ScaleData
539 command (while regressing out mitochondrial genes) for the Principal Component Analysis (PCA),
540 which was performed by the RunPCA command for 30 PCs. After integration with Harmony[61], the
541 data was subsequently processed with Louvain clustering and dimensionality reduction via
542 Uniform Manifold Approximation and Projection (UMAP) using 30 principal components, reduction
543 = "harmony", and resolution of 0.8, to visualize nuclear transcriptomic profiles in two-dimensional
544 space. For annotation, we used the Allen Brain Cell (ABC) Atlas tool MapMyCells
545 (RRID:SCR_024672, the reference taxonomy: 10x Whole Mouse Brain (CCN20230722),
546 mapping algorithm: hierarchical mapping)[23] to assign neuronal classes or subclasses to nuclei
547 from a whole dataset. To validate the classification, we examined the clusters using well-
548 established markers such as *Th*, *Slc17a6* (Vglut2), and *Slc32a1* (Vgat), which confirmed that the
549 annotation was reasonable. To subset the dopaminergic population, we first used the annotation
550 (21_MB_Dopa) to identify and extract the relevant population. We then re-scaled the extracted
551 data and applied the supertype or cluster annotation to the subset and performed further analysis.
552 Differentially expressed genes in each cluster were identified by Wilcoxon test (the FindAllMarkers
553 function in Seurat),
554
555 **Differential cell abundance**
556 To identify differentially abundant cell populations in each dataset, we used two methods: MASC
557 (version 0.10)[24] and Milo (version 1.99)[30]. MASC is a single cell association method for testing
558 whether a certain status influences the membership of single cells while accounting for technical
559 confounds and biological variation. For all datasets, we included sex as a fixed effect, and
560 individual as a random effect in the model. We then tested the significance of association between
561 the status (i.e. MitoPark mice and their littermate controls at each stage, or MitoPark mice at
562 different stages) with the clusters. Cell subpopulations were considered significantly associated
563 with a status at FDR-adjusted P<0.05 and absolute odds ratio >0. Milo constructs local
564 neighborhoods (k=30, d=30) of transcriptionally similar cells on a k-nearest neighbor (kNN) graph
565 derived from the single-cell dataset, effectively grouping small clusters of similar cells together.
566 Each neighborhood represents a subset of cells with comparable transcriptomic profiles and may

567 correspond to fine-grained cellular subpopulations. Milo then quantifies the number of cells from
568 each sample within each neighborhood and compares their relative abundances across
569 experimental conditions, for example, assessing whether certain neighborhoods are enriched in
570 diseased samples relative to healthy controls. Statistical testing is performed to determine
571 whether these differences are significant or attributable to random variation. By systematically
572 applying this procedure across all neighborhoods, Milo identifies cellular subpopulations that
573 exhibit condition-specific changes in abundance.
574
575 **Gene ontology enrichment analysis**
576 We used the g:Profiler web tool and gprofiler2 R package (version 0.2.3)[62] to identify significantly
577 enriched gene ontology (GO) terms from upregulated or downregulated gene lists in dopaminergic
578 clusters.
579
580 **Stereotaxic viral injections**
581 Before starting the surgery mice were subcutaneously injected with Buprenorphine XR (0.5–1 mg
582 per kg body weight). The mouse head was shaved, cleaned with 70% alcohol and iodine, an
583 intradermic injection of bupivacaine (2 mg per kg body weight) was administered, and a small
584 incision from anterior to posterior was made on the skin to allow for aligning the head and drilling
585 the hole for the injection site. Surgeries were performed under sterile conditions and isoflurane
586 (1%–5%, plus oxygen at 1-1.5 l/min) anesthesia on a motorized stereotactic frame (David Kopf
587 Instruments, Model 900SD). Throughout each surgery, mouse body temperature was maintained
588 at 37C using an animal temperature controller (ATC2000, World Precision Instruments). For
589 anterograde tracing experiments, animal were unilaterally injected with 300nL of AAV5-CAG-
590 FLEX-GFP (titer: 4.5E12 vg/mL; UNC Vector Core) into the right hemisphere of the substantia
591 nigra pars compacta (SNc; AP -3.16 mm, ML 1.3 mm, DV -4.0 mm) using a Nanoject III Injector
592 (Drummond Scientific, USA) at a pulse rate of 5.1 nL per second, 20 nL per pulse every 5 s. After
593 injection, the pipette was held in place for 5 minutes before raising to ensure minimize viral efflux.
594 For whole-brain retrograde tracing experiments using rabies virus, 100nL of a 2:1 mixture of the
595 helper viruses, AAV1-CAG-FLEX-N2cG-mKate2.0 (titer: 9.83E12 vg/mL; Janelia Viral Core) or
596 AAVDJ-CAG-FlpX-N2cG-mKate2.0 (titer: 2.60E12 vg/mL; Zuckerman Institute Vector Core) and
597 AAV5-Esyn-DIO-TVA950-EYFP-WPRE (titer: 1.44E13 vg/mL; Salk Viral Vector Core), was
598 injected into the SNc. Two weeks later, 300nl of EnvA-N2c-deltaG-tdTomato (titer: 1.5E9 ffu/ml;
599 Center for Neuroanatomy with Neurotropic Viruses, CNNV) was injected within the same area at
600 a 10-degree angle (SNc; AP -3.16 mm, ML 2.0mm, DV -4.0 mm) to prevent labeling the injection

601 tract with TVA. For monosynaptic labeling from the primary motor cortex or the dorsal striatum,
602 100nL of a 2:1 mixture of the helper viruses, AAV1-CAG-FLEX-N2cG-mKate2.0 (titer: 9.83E12
603 vg/mL; Janelia Viral Core) and AAV5-Esyn-DIO-TVA950-EYFP-WPRE (titer: 1.44E13 vg/mL;
604 Salk Viral Vector Core), was injected into the SNc. 100nL of AAVDJ-Ef1a-fDIO-mScarlet (titer:
605 6.30E12 vg/mL; Zuckerman Institute Vector Core) was injected in the motor cortex or the striatum.
606 Two weeks later, 300nl of EnvA-N2c-deltaG-H2B-HA-FlpO (titer: 1.0E9 ffu/ml; Zuckerman
607 Institute Vector Core) was injected within the same area at a 10-degree angle (SNc; AP -3.16 mm,
608 ML 2.0mm, DV -4.0 mm). After the injection, the skull was cleaned and the skin sealed with
609 sutures and Vetbond tissue adhesive (3M, Maplewood, MN, USA). For ablation experiments, 150
610 nL of AAV5-EF1a-FLEX-taCasp3-TEVp virus (titer 4.20E12 vg/mL; UNC Vector Core) was
611 bilaterally injected into the SNc of DAT-Cre at two specific coordinates (SNc-medial: AP -3.16
612 mm, ML 1.10 mm, DV -4.1 mm; SNc-lateral: AP -3.16 mm, ML 1.50 mm, DV -4.1 mm). These
613 coordinates effectively targeted and ablated SNc dopaminergic neurons. For silencing
614 neurotransmission, 300nL of AAVDJ-hSyn-FLEX-TeLC-EYFP (titer 7.40E12 vg/mL; Zuckerman
615 Institute Vector Core) was bilaterally injected in the SNc of Anxa1-Cre (SNc; AP -3.16 mm, ML
616 1.3 mm, DV -4.0 mm).
617
618 **Open field and cylinder test behavior assays**
619 Mice were habituated with a wireless motion sensor in a square arena (40 x 40 x 20 cm, length x
620 width x height) housed inside a sound-attenuating chamber for 30 minutes on the first day.
621 Imaging was conducted using a 1280 x 1024 pixel FLIR camera (Point Grey Flea) with a CS
622 mount lens, recording at 30 Hz. For the open-field test, mice were imaged for 30 minutes from a
623 top view, and for the cylinder test (a cylinder arena: 15cm diameter x 30cm length), they were
624 imaged for 15 minutes from a side view. Video acquisition was performed using the commercial
625 software FlyCapture and the open-source visual language Bonsai[63]. Mouse centroid coordinates
626 (i.e., spine2 in DeepLabCut tracking, details provided below) during the open-field recording were
627 used to calculate basic measures of activity (e.g., trajectory or velocity). Acceleration data was
628 collected at a sampling rate of 200 Hz (details provided below).
629
630 **Pose estimation and tracking analysis**
631 DeepLabCut[64] was used to estimate the pose of the mice and track their movements throughout
632 the trials. In the open-field test, seven body parts (nose, right ear, left ear, spine1, spine2, spine3,
633 tail) were labeled to create a skeleton for pose estimation. For the cylinder test, two body parts
634 (motion sensor and nose) were labeled. A total of 1,100 frames were labeled for the open-field

test (training: 1.03 million iterations, training error: 1.72 pixels, test error: 2.76 pixels), and 1,040 frames were labeled for the cylinder test (training: 1.03 million iterations, training error: 2.31 pixels, test error: 6.8 pixels). The pose data was filtered using a median filter and verified through visual inspection. For the analysis in the open-field test, to ensure consistent data, we only used data from the 5 to 20-minute mark (15 minutes total) within a 30-minute recording, as mice tend to move differently during the first few minutes after being placed from their home cage into the field. Immobility was defined as any tracking point with a speed of less than 0.5 cm/s for a duration of more than 0.5 seconds, and estimates with a likelihood lower than 0.95 were excluded. Average speed was calculated only during periods when the animal was mobile. In the cylinder test, the full 15 minutes of data were used for analysis, since mice often exhibit exploratory rearing behaviors during the first few minutes. For quantifying the number of rears, we tracked the vertical positions of the nose and motion sensor on the mouse head using DeepLabCut. If the tracking was sustained for at least 0.5 seconds in the same position, it was defined as a single rearing behavior. The height thresholds were determined using DeepLabCut's output (i.e., filtered trajectory plots), and the number of rears instances was recorded.

Motion sensor acceleration data analysis

Wireless motion sensor data was collected using the WEAR system developed by the Champalimaud Hardware Platform. The sensor is compact and lightweight (~1.8 g), capable of sampling nine-axis motion data from a three-axis accelerometer, gyroscope, and magnetometer at rates up to 200 Hz[15]. This device communicates with computers through a base station designed by the platform, utilizing the Harp system. The base station is accessible via a software GUI (e.g., Harp Wear), allowing for easy adjustment of sensor parameters to best fit experimental needs. Additionally, it is compatible with Bonsai software[63], enabling synchronization of the WEAR sensor data with other data sources, such as cameras. The data was first filtered using a 5th order, 1Hz low-pass Butterworth filter to separate the gravitational acceleration component of each axis. This component was then subtracted to the original acceleration data to obtain the fast acceleration changes induced by mice's movements (body acceleration). Total body acceleration was determined by calculating the vector norm of the three body acceleration axis. To assess the emergence of rhythmic, oscillatory movements, we performed a spectral analysis of the body's dorso-ventral acceleration axis. We used the signal.spectrogram function of the Scipy python library[65] to calculate a spectrogram with consecutive Fourier transforms, using segments of 256 samples with a 50% overlap. The spectrogram was normalized by transforming the power values of each window to a 0-1 range (maximum= 1 and minimum=0). For each mouse a final measure

669 was obtained by calculating the median normalized power considering all the windows of the
670 spectrogram.
671
672 **Pavlovian conditioning**
673 Mice were habituated to custom-made Pavlovian chambers (17 x 14 x 20 cm, length x width x
674 height) placed inside sound-attenuating boxes. They were food-restricted throughout the training
675 period and maintained at 85% of their original body weight. Each chamber was equipped with a
676 nose poke port featuring an infrared beam and stimulus LED, as well as a speaker. A food reward
677 (6-8 µl of 10% sucrose solution) was delivered through a magazine spout equipped with a
678 lickometer. Cues and reward delivery were controlled by a Python-based framework (i.e., the
679 pyControl system[66]), which also recorded all behavioral timestamps. Behavior was monitored
680 using top (USB camera, ELP, China) and side (Flea3, FLIR, USA) cameras, with video capture
681 managed by FlyCapture and Bonsai softwares. For stimuli, a 10-second LED light served as the
682 CS+, while a 10-second tone (4 kHz, 75 dB) served as the CS-. At the onset of each CS+, a drop
683 of sucrose solution was delivered to the tip of the spout, whereas the CS- was not paired with a
684 reward. CS+ and CS- were presented independently on a random inter-trial interval schedule of
685 120 seconds (ITI = RI-120). A training session concluded once the animal received a total of 30
686 rewards. Each animal underwent one training session per day for five consecutive days. Learning
687 progress was assessed by monitoring the lick rate and the latency for each mouse to make its
688 first lick after the onset of each CS+.
689
690 **Histology**
691 Mice were deeply anesthetized with isoflurane and transcardially perfused with PBS, followed by
692 ice-cold 4% paraformaldehyde. Brains were then removed for histological analysis. Coronal
693 sections were cut at 30 µm for immunostaining or 75 µm for 3D reconstruction using a Leica
694 VT1000 vibratome. The tissue was rinsed twice in 1x PBS and then permeabilized in PBS
695 containing 0.4% Triton X-100 (PBST). For quantification of *Th*+ cells in MitoPark mice and Anxa1-
696 Cre mouse line, immunohistochemistry was performed with primary antibodies by incubating the
697 sections with an anti-GFP antibody (Chicken, Aves labs Inc, GFP-1020) and a TH antibody
698 (Mouse, ImmunoStar, 22941) diluted at 1:2000 in 0.4% Triton X-100 PBS (PBST) overnight at 4C.
699 To visualize the dorsal-tier or ventral-tier of the SNc DANs, we also used a Calbindin D28K (Rabbit,
700 Synaptic Systems, 214002) or an Aldh1a1 antibody (Goat, R&D Systems, AF5869). The sections
701 were then incubated with secondary antibodies (Donkey anti-Chicken Alexa Fluor 488,
702 JacksonImmunoResearch, 703-545-155; Donkey anti-Goat Alexa Fluor 568, Invitrogen, A11057;

703 Donkey anti-Rabbit Alexa Fluor 568 (Invitrogen, A10042); Donkey anti-Mouse Alexa Fluor 647,
704 Invitrogen, A31571) diluted at 1:2000 in 0.4% PBST overnight at 4C. DAPI (Sigma D9542; 1:1000)
705 was used as a counterstain in all experiments.
706
707 **Image acquisition, processing, and analysis**
708 Coronal sections (30µm or 75µm) were serially mounted on slides and sections were imaged
709 using an automated slide scanner (Nikon AZ100 Multizoom microscope) equipped with a 4x
710 0.4NA Plan Apo objective (Nikon Instruments Inc) and P200 slide loader (Prior Scientific),
711 controlled by NIS-Elements using custom acquisition scripts (Nikon Instruments Inc.). Image
712 processing and analysis using BrainJ proceeded as previously described[21]. Briefly, brain sections
713 were aligned and registered using two-dimensional (2D) rigid-body registration. After background
714 subtraction ilastik was used to detect cell bodies and neuronal processes[67]. Probability images
715 for class (soma and neuronal processes) were generated using the pixel classification approach
716 in ilastik, ensuring improved accuracy for segmentation over fluorescence intensity alone. To map
717 the location of these structures to an annotated brain atlas, serial tissue sections were registered
718 into a single volume before 3D registration to the template brain (Allen Brain Atlas Common
719 Coordinate Framework) using Elastix[68]. Initial measurements and data visualization were
720 performed in ImageJ, and subsequent analyses were performed in Python.
721
722 **Statistics and reproducibility**
723 All statistical analyses were conducted using R or Python. Data are presented as mean with 95%
724 confidence intervals (CI) or as the standard error of the mean (SEM), unless otherwise specified.
725 Statistical significance was assessed using a two-sided Mann–Whitney U test, and for multiple
726 comparisons, a two-way ANOVA followed by Tukey's HSD test was applied. To further validate
727 the results, a linear mixed-effects model (LMM) with Tukey's post hoc comparisons was also
728 conducted for certain results (*$p < 0.05$, **$p < 0.01$, ***$p < 0.001$, ****$p < 0.0001$). All
729 measurements were obtained from distinct, independent samples unless otherwise stated.
730
731 **Data and code availability**
732 All data, code, experimental protocols, and essential laboratory materials used or generated in
733 this study are listed in the Key Resources Table, together with their corresponding persistent
734 identifiers at DOI: 10.5281/zenodo.18273548.
735
736 **Acknowledgments**

We would like to thank Zuckerman Institute's Cellular Imaging platform for providing instrument use and technical advice. Special thanks to Gabriela J. Martins, Mariana L. Correia and Helena M Seuffert for mouse maintenance and Drew Baughman, Mafalda Vicente and Chrissy Weber-Schmidt for additional support with lab and mouse management. We also appreciate Helio Rodrigues for designing and constructing behavioral equipment, and Kim Ritola for creating custom viral constructs. Our gratitude extends to Ira Schieren for assisting with FACS sorting. This work was supported by grants from the Aligning Science Across Parkinson's (ASAP-020551) through the Michael J. Fox Foundation for Parkinson's Research (MJFF), the Parkinson's Disease Foundation (PDFPF-RCE-1948), the National Institutes of Health (NIH, U19: 5U19NS104649-03), and a NARSAD Young Investigator Grant from the Brain & Behavior Research Foundation (30086). This research was funded in part through the NIH/NCI Cancer Center Support Grant P30CA013696 and used the Genomics and High Throughput Screening Shared Resource. Additional support was received from the National Center for Advancing Translational Sciences, NIH, under Grant Number UL1TR001873. Rabies viruses were produced by the Center for Neuroanatomy with Neurotropic Viruses (CNNV), supported by the NIH under Grant P40 OD010996. For the purpose of open access, the author has applied a CC BY public copyright license to all Author Accepted Manuscripts arising from this submission.

Author contributions

A.F. and R.M.C. designed the study, interpreted the results, and wrote the manuscript. A.F. conducted the experiments and analyzed the data. D.N. generated viral constructs and assisted with the production of transgenic mice. Z.R.L., A.Y., B.T., and V.M. contributed to transcriptome data analysis and interpretation of sequencing results. L.A.H. developed the automated pipeline for anatomical reconstruction and analysis, and contributed to histological assessments. C.W. produced the rabies virus. T.S. and J.A.d.S. assisted with accelerometer experiments and data analysis. R.M.C. supervised the project. All authors contributed to the interpretation of results and manuscript editing.

Declaration of interests

The authors declare no competing interests.

References

769 1. Barrett, M.J., Wylie, S.A., Harrison, M.B., and Wooten, G.F. (2011). Handedness and
770 motor symptom asymmetry in Parkinson's disease. J. Neurol. Neurosurg. Psychiatry *82*,
771 1122–1124. https://doi.org/10.1136/jnnp.2010.209783.
772 2. Hirsch, E.C., Graybiel, A.M., and Agid, Y. (1988). Melanized dopaminergic neurons are
773 differentially affected in Parkinson's disease. Nature *334*, 345--348.
774 3. HORNYKIEWICZ, O. (1963). [The tropical localization and content of noradrenalin and
775 dopamine (3-hydroxytyramine) in the substantia nigra of normal persons and patients
776 with Parkinson's disease]. Wien. Klin. Wochenschr. *75*, 309—312.
777 4. Poulin, J.F., Gaertner, Z., Moreno-Ramos, O.A., and Awatramani, R. (2020).
778 Classification of Midbrain Dopamine Neurons Using Single-Cell Gene Expression
779 Profiling Approaches. Trends Neurosci. *43*, 155–169.
780 https://doi.org/10.1016/j.tins.2020.01.004.
781 5. Azcorra, M., Gaertner, Z., Davidson, C., He, Q., Kim, H., Nagappan, S., Hayes, C.K.,
782 Ramakrishnan, C., Fenno, L., Kim, Y.S., et al. (2023). Unique functional responses
783 differentially map onto genetic subtypes of dopamine neurons. Nat. Neurosci. *26*, 1762–
784 1774. https://doi.org/10.1038/s41593-023-01401-9.
785 6. Poulin, J.F., Caronia, G., Hofer, C., Cui, Q., Helm, B., Ramakrishnan, C., Chan, C.S.,
786 Dombeck, D.A., Deisseroth, K., and Awatramani, R. (2018). Mapping projections of
787 molecularly defined dopamine neuron subtypes using intersectional genetic approaches.
788 Nat. Neurosci. *21*, 1260–1271. https://doi.org/10.1038/s41593-018-0203-4.
789 7. Damier, P., Hirsch, E.C., Agid, Y., and Graybiel, A.M. (1999). The substantia nigra of the
790 human brain: II. Patterns of loss of dopamine-containing neurons in Parkinson's disease.
791 Brain *122*, 1437–1448. https://doi.org/10.1093/brain/122.8.1437.
792 8. Kamath, T., Abdulraouf, A., Burris, S.J., Langlieb, J., Gazestani, V., Nadaf, N.M.,
793 Balderrama, K., Vanderburg, C., and Macosko, E.Z. (2022). Single-cell genomic profiling
794 of human dopamine neurons identifies a population that selectively degenerates in
795 Parkinson's disease (Springer US) https://doi.org/10.1038/s41593-022-01061-1.
796 9. Spillantini, M.G., Schmidt, M.L., Lee, V.M.-Y., Trojanowski, J.Q., Jakes, R., and Goedert,
797 M. (1997). α-Synuclein in Lewy bodies. Nature *388*, 839–840.
798 https://doi.org/10.1038/42166.
799 10. Kitada, T., Asakawa, S., Hattori, N., Matsumine, H., Yamamura, Y., Minoshima, S.,
800 Yokochi, M., Mizuno, Y., and Shimizu, N. (1998). Mutations in the parkin gene cause
801 autosomal recessive juvenile parkinsonism. Nature *392*, 605–608.
802 https://doi.org/10.1038/33416.
803 11. Schapira, A.H. V, Cooper, J.M., Dexter, D., Clark, J.B., Jenner, P., and Marsden, C.D.
804 (1990). Mitochondrial Complex I Deficiency in Parkinson's Disease. J. Neurochem. *54*,
805 823–827. https://doi.org/https://doi.org/10.1111/j.1471-4159.1990.tb02325.x.
806 12. González-Rodríguez, P., Zampese, E., Stout, K.A., Guzman, J.N., Ilijic, E., Yang, B.,
807 Tkatch, T., Stavarache, M.A., Wokosin, D.L., Gao, L., et al. (2021). Disruption of
808 mitochondrial complex I induces progressive parkinsonism. Nature *599*, 650–656.
809 https://doi.org/10.1038/s41586-021-04059-0.
810 13. Ekstrand, M.I., Terzioglu, M., Galter, D., Zhu, S., Hofstetter, C., Lindqvist, E., Thams, S.,
811 Bergstrand, A., Hansson, F.S., Trifunovic, A., et al. (2007). Progressive parkinsonism in

812 mice with respiratory-chain-deficient dopamine neurons. Proc. Natl. Acad. Sci. U. S. A.
813 *104*, 1325–1330. https://doi.org/10.1073/pnas.0605208103.
814 14. Beckstead, M.J., and Howell, R.D. (2021). Progressive parkinsonism due to mitochondrial
815 impairment: Lessons from the MitoPark mouse model. Exp. Neurol. *341*.
816 https://doi.org/10.1016/j.expneurol.2021.113707.
817 15. Da Silva, J.A., Tecuapetla, F., Paixão, V., and Costa, R.M. (2018). Dopamine neuron
818 activity before action initiation gates and invigorates future movements. Nature *554*, 244–
819 248. https://doi.org/10.1038/nature25457.
820 16. Crabtree, D.M., and Zhang, J. (2012). Genetically engineered mouse models of
821 Parkinson's disease. Brain Res. Bull. *88*, 13–32.
822 https://doi.org/10.1016/j.brainresbull.2011.07.019.
823 17. Bhatia, K.P., Bain, P.G., Bajaj, N.P.S., Elble, R.J., Hallett, M., Louis, E.D., Raethjen, J.,
824 Stamelou, M., Testa, C.M., and Deuschl, G. (2018). Consensus Statement on the
825 classification of tremors. from the task force on tremor of the International Parkinson and
826 Movement Disorder Society. Movement Disorders *33*.
827 18. Yang, C.F., Chiang, M.C., Gray, D.C., Prabhakaran, M., Alvarado, M., Juntti, S.A., Unger,
828 E.K., Wells, J.A., and Shah, N.M. (2013). Sexually dimorphic neurons in the ventromedial
829 hypothalamus govern mating in both sexes and aggression in males. Cell *153*, 896–909.
830 https://doi.org/10.1016/j.cell.2013.04.017.
831 19. Wang, Q., Ding, S.L., Li, Y., Royall, J., Feng, D., Lesnar, P., Graddis, N., Naeemi, M.,
832 Facer, B., Ho, A., et al. (2020). The Allen Mouse Brain Common Coordinate Framework:
833 A 3D Reference Atlas. Cell *181*, 936-953.e20. https://doi.org/10.1016/j.cell.2020.04.007.
834 20. Hintiryan, H., Foster, N.N., Bowman, I., Bay, M., Song, M.Y., Gou, L., Yamashita, S.,
835 Bienkowski, M.S., Zingg, B., Zhu, M., et al. (2016). The mouse cortico-striatal projectome.
836 Nat. Neurosci. *19*, 1100–1114. https://doi.org/10.1038/nn.4332.
837 21. Botta, P., Fushiki, A., Vicente, A.M., Hammond, L.A., Mosberger, A.C., Gerfen, C.R.,
838 Peterka, D., and Costa, R.M. (2020). An Amygdala Circuit Mediates Experience-
839 Dependent Momentary Arrests during Exploration. Cell *183*, 605-619.e22.
840 https://doi.org/10.1016/j.cell.2020.09.023.
841 22. Allen Institute for Brain Science Isolation of Nuclei from Adult Mouse Brain Tissue
842 Protocol V.2. https://doi.org/dx.doi.org/10.17504/protocols.io.bq7emzje.
843 23. Yao, Z., van Velthoven, C.T.J., Kunst, M., Zhang, M., McMillen, D., Lee, C., Jung, W.,
844 Goldy, J., Abdelhak, A., Aitken, M., et al. (2023). A high-resolution transcriptomic and
845 spatial atlas of cell types in the whole mouse brain. Nature *624*, 317–332.
846 https://doi.org/10.1038/s41586-023-06812-z.
847 24. Fonseka, C.Y., Rao, D.A., Teslovich, N.C., Korsunsky, I., Hannes, S.K., Slowikowski, K.,
848 Gurish, M.F., Donlin, L.T., Lederer, J.A., Weinblatt, M.E., et al. (2018). Mixed-effects
849 association of single cells identifies an expanded effector CD4+ T cell subset in
850 rheumatoid arthritis. Sci. Transl. Med. *10*. https://doi.org/10.1126/scitranslmed.aaq0305.
851 25. Steinkellner, T., Conrad, W.S., Kovacs, I., Rissman, R.A., Lee, E.B., Trojanowski, J.Q.,
852 Freyberg, Z., Roy, S., Luk, K.C., Lee, V.M., et al. (2022). Dopamine neurons exhibit
853 emergent glutamatergic identity in Parkinson's disease. Brain *145*, 879–886.
854 https://doi.org/10.1093/brain/awab373.

855 26. Shen, H., Marino, R.A.M., McDevitt, R.A., Bi, G.H., Chen, K., Madeo, G., Lee, P.T.,
856 Liang, Y., De Biase, L.M., Su, T.P., et al. (2018). Genetic deletion of vesicular glutamate
857 transporter in dopamine neurons increases vulnerability to MPTP-induced neurotoxicity in
858 mice. Proc. Natl. Acad. Sci. U. S. A. *115*, E11532–E11541.
859 https://doi.org/10.1073/pnas.1800886115.
860 27. Pereira Luppi, M., Azcorra, M., Caronia-Brown, G., Poulin, J.F., Gaertner, Z., Gatica, S.,
861 Moreno-Ramos, O.A., Nouri, N., Dubois, M., Ma, Y.C., et al. (2021). Sox6 expression
862 distinguishes dorsally and ventrally biased dopamine neurons in the substantia nigra with
863 distinctive properties and embryonic origins. Cell Rep. *37*.
864 https://doi.org/10.1016/j.celrep.2021.109975.
865 28. Panman, L., Andersson, E., Alekseenko, Z., Hedlund, E., Kee, N., Mong, J., Uhde, C.W.,
866 Deng, Q., Sandberg, R., Stanton, L.W., et al. (2011). Transcription factor-induced lineage
867 selection of stem-cell-derived neural progenitor cells. Cell Stem Cell *8*, 663–675.
868 https://doi.org/10.1016/j.stem.2011.04.001.
869 29. Panman, L., Papathanou, M., Laguna, A., Oosterveen, T., Volakakis, N., Acampora, D.,
870 Kurtsdotter, I., Yoshitake, T., Kehr, J., Joodmardi, E., et al. (2014). Sox6 and Otx2 control
871 the specification of substantia nigra and ventral tegmental area dopamine neurons. Cell
872 Rep. *8*, 1018–1025. https://doi.org/10.1016/j.celrep.2014.07.016.
873 30. Dann, E., Henderson, N.C., Teichmann, S.A., Morgan, M.D., and Marioni, J.C. (2022).
874 Differential abundance testing on single-cell data using k-nearest neighbor graphs. Nat.
875 Biotechnol. *40*, 245–253. https://doi.org/10.1038/s41587-021-01033-z.
876 31. Yu, Z., Guindani, M., Grieco, S.F., Chen, L., Holmes, T.C., and Xu, X. (2022). Beyond t
877 test and ANOVA: applications of mixed-effects models for more rigorous statistical
878 analysis in neuroscience research. Neuron *110*, 21–35.
879 https://doi.org/10.1016/j.neuron.2021.10.030.
880 32. Liu, G., Yu, J., Ding, J., Xie, C., Sun, L., Rudenko, I., Zheng, W., Sastry, N., Luo, J.,
881 Rudow, G., et al. (2014). Aldehyde dehydrogenase 1 defines and protects a nigrostriatal
882 dopaminergic neuron subpopulation. Journal of Clinical Investigation *124*, 3032–3046.
883 https://doi.org/10.1172/JCI72176.
884 33. Sgobio, C., Sun, L., Ding, J., Herms, J., Lovinger, D.M., and Cai, H. (2019). Unbalanced
885 calcium channel activity underlies selective vulnerability of nigrostriatal dopaminergic
886 terminals in Parkinsonian mice. Sci. Rep. *9*. https://doi.org/10.1038/s41598-019-41091-7.
887 34. Wu, J., Kung, J., Dong, J., Chang, L., Xie, C., Habib, A., Hawes, S., Yang, N., Chen, V.,
888 Liu, Z., et al. (2019). Distinct Connectivity and Functionality of Aldehyde Dehydrogenase
889 1a1-Positive Nigrostriatal Dopaminergic Neurons in Motor Learning. Cell Rep. *28*, 1167-
890 1181.e7. https://doi.org/10.1016/j.celrep.2019.06.095.
891 35. Albarran, E., Fushiki, A., Nelson, A., Ng, D., Chaimowitz, C., Nikoobakht, L., Sippy, T.,
892 Peterka, D.S., and Costa, R.M. (2025). Generation of knock-in Cre and FlpO mouse lines
893 for precise targeting of striatal projection neurons and dopaminergic neurons.
894 https://doi.org/10.7554/eLife.108458.1.
895 36. Reardon, T.R., Murray, A.J., Turi, G.F., Wirblich, C., Croce, K.R., Schnell, M.J., Jessell,
896 T.M., and Losonczy, A. (2016). Rabies Virus CVS-N2cδG Strain Enhances Retrograde
897 Synaptic Transfer and Neuronal Viability. Neuron *89*, 711–724.
898 https://doi.org/10.1016/j.neuron.2016.01.004.

37. Watabe-Uchida, M., Zhu, L., Ogawa, S.K., Vamanrao, A., and Uchida, N. (2012). Whole-Brain Mapping of Direct Inputs to Midbrain Dopamine Neurons. Neuron *74*, 858–873. https://doi.org/10.1016/j.neuron.2012.03.017.
38. Menegas, W., Bergan, J.F., Ogawa, S.K., Isogai, Y., Venkataraju, K.U., Osten, P., Uchida, N., and Watabe-Uchida, M. (2015). Dopamine neurons projecting to the posterior striatum form an anatomically distinct subclass. Elife *4*, 2014–2016. https://doi.org/10.7554/eLife.10032.
39. Zhang, Y., Zhao, S., Rodriguez, E., Takatoh, J., Han, B.X., Zhou, X., and Wang, F. (2015). Identifying local and descending inputs for primary sensory neurons. Journal of Clinical Investigation *125*, 3782–3794. https://doi.org/10.1172/JCI81156.
40. Poewe, W., Seppi, K., Tanner, C.M., Halliday, G.M., Brundin, P., Volkmann, J., Schrag, A.E., and Lang, A.E. (2017). Parkinson disease. Nat. Rev. Dis. Primers *3*, 1–21. https://doi.org/10.1038/nrdp.2017.13.
41. Li, X., Redus, L., Chen, C., Martinez, P.A., Strong, R., Li, S., and O'Connor, J.C. (2013). Cognitive Dysfunction Precedes the Onset of Motor Symptoms in the MitoPark Mouse Model of Parkinson's Disease. PLoS One *8*, e71341. https://doi.org/10.1371/journal.pone.0071341.
42. Abusrair, A.H., Elsekaily, W., and Bohlega, S. (2022). Tremor in Parkinson's Disease: From Pathophysiology to Advanced Therapies. Tremor and Other Hyperkinetic Movements *12*. https://doi.org/10.5334/tohm.712.
43. Handforth, A. Harmaline Tremor: Underlying Mechanisms in a Potential Animal Model of Essential Tremor.
44. Nicoletti, V., Cecchi, P., Pesaresi, I., Frosini, D., Cosottini, M., and Ceravolo, R. (2020). Cerebello-thalamo-cortical network is intrinsically altered in essential tremor: evidence from a resting state functional MRI study. Sci. Rep. *10*, 16661. https://doi.org/10.1038/s41598-020-73714-9.
45. Claassen, D.O., McDonell, K.E., Donahue, M., Rawal, S., Wylie, S.A., Neimat, J.S., Kang, H., Hedera, P., Zald, D., Landman, B., et al. (2016). Cortical asymmetry in Parkinson's disease: early susceptibility of the left hemisphere. Brain Behav. *6*. https://doi.org/10.1002/brb3.573.
46. Mendonça, M.D., Ferreira, P.C., Oliveira, F., Barbosa, R., Meira, B., Costa, D.C., Oliveira-Maia, A.J., and da Silva, J.A. (2024). Relative sparing of dopaminergic terminals in the caudate nucleus is a feature of rest tremor in Parkinson's disease. NPJ Parkinsons Dis. *10*. https://doi.org/10.1038/s41531-024-00818-8.
47. Yaghmaeian Salmani, B., Lahti, L., Gillberg, L., Jacobsen, J.K., Mantas, I., Svenningsson, P., and Perlmann, T. (2024). Transcriptomic atlas of midbrain dopamine neurons uncovers differential vulnerability in a Parkinsonism lesion model. Elife *12*. https://doi.org/10.7554/elife.89482.
48. Mantas, I., Contestabile, A., Skara, V., Loiseau, C., Santos, I.A., Cramb, K.M.L., Filograna, R., Wade-Martins, R., Magill, P., and Meletis, K. (2024). Anxa1+ dopamine neuron vulnerability defines prodromal Parkinson's disease bradykinesia and procedural motor learning impairment. https://doi.org/10.1101/2024.12.22.629963.
49. Hadjas, L.C., Kollman, G.J., Linderhof, L., Xia, M., Mansur, S., Saint-Pierre, M., Lim, B.K., Lee, E.B., Cicchetti, F., Awatramani, R., et al. (2025). Parkinson's Disease-vulnerable

943 and -resilient dopamine neurons display opposite responses to excitatory input.
944 https://doi.org/10.1101/2025.06.03.657460.
945 50. Crittenden, J.R., Tillberg, P.W., Riad, M.H., Shima, Y., Gerfen, C.R., Curry, J., Housman,
946 D.E., Nelson, S.B., Boyden, E.S., and Graybiel, A.M. (2016). Striosome-dendron
947 bouquets highlight a unique striatonigral circuit targeting dopamine-containing neurons.
948 Proc. Natl. Acad. Sci. U. S. A. *113*, 11318–11323.
949 https://doi.org/10.1073/pnas.1613337113.
950 51. Evans, R.C., Twedell, E.L., Zhu, M., Ascencio, J., Zhang, R., and Khaliq, Z.M. (2020).
951 Functional Dissection of Basal Ganglia Inhibitory Inputs onto Substantia Nigra
952 Dopaminergic Neurons. Cell Rep. *32*, 108156.
953 https://doi.org/10.1016/j.celrep.2020.108156.
954 52. Eschbach, C., Fushiki, A., Winding, M., Schneider-Mizell, C.M., Shao, M., Arruda, R.,
955 Eichler, K., Valdes-Aleman, J., Ohyama, T., Thum, A.S., et al. (2020). Recurrent
956 architecture for adaptive regulation of learning in the insect brain. Nat. Neurosci. *23*, 544–
957 555. https://doi.org/10.1038/s41593-020-0607-9.
958 53. Xu, Z., Feng, Z., Zhao, M., Sun, Q., Deng, L., Jia, X., Jiang, T., Luo, P., Chen, W., Tudi,
959 A., et al. Whole-brain connectivity atlas of glutamatergic and GABAergic neurons in the
960 mouse dorsal and median raphe nuclei. https://doi.org/10.7554/eLife.
961 54. Bolduc, C., Oram, C., Donovan, S., Bach, H., Liu, M., Marier, R., Sharpe, M., Campeau,
962 C., Spencer, C.D., Martin, S.A., et al. (2025). Calbindin Stratifies Midbrain Dopaminergic
963 Neurons Governing Distinct Aspects of Locomotion.
964 https://doi.org/10.1101/2025.07.07.663227.
965 55. Tasic, B., Menon, V., Nguyen, T.N., Kim, T.K., Jarsky, T., Yao, Z., Levi, B., Gray, L.T.,
966 Sorensen, S.A., Dolbeare, T., et al. (2016). Adult mouse cortical cell taxonomy revealed
967 by single cell transcriptomics. Nat. Neurosci. *19*, 335–346.
968 https://doi.org/10.1038/nn.4216.
969 56. Tasic, B., Yao, Z., Graybuck, L.T., Smith, K.A., Nguyen, T.N., Bertagnolli, D., Goldy, J.,
970 Garren, E., Economo, M.N., Viswanathan, S., et al. (2018). Shared and distinct
971 transcriptomic cell types across neocortical areas. Nature *563*, 72–78.
972 https://doi.org/10.1038/s41586-018-0654-5.
973 57. Schneider, V.A., Graves-Lindsay, T., Howe, K., Bouk, N., Chen, H.C., Kitts, P.A., Murphy,
974 T.D., Pruitt, K.D., Thibaud-Nissen, F., Albracht, D., et al. (2017). Evaluation of GRCh38
975 and de novo haploid genome assemblies demonstrates the enduring quality of the
976 reference assembly. Genome Res. *27*, 849–864. https://doi.org/10.1101/gr.213611.116.
977 58. Hao, Y., Stuart, T., Kowalski, M.H., Choudhary, S., Hoffman, P., Hartman, A., Srivastava,
978 A., Molla, G., Madad, S., Fernandez-Granda, C., et al. (2024). Dictionary learning for
979 integrative, multimodal and scalable single-cell analysis. Nat. Biotechnol. *42*, 293–304.
980 https://doi.org/10.1038/s41587-023-01767-y.
981 59. Young, M.D., and Behjati, S. (2020). SoupX removes ambient RNA contamination from
982 droplet-based single-cell RNA sequencing data. Gigascience *9*.
983 https://doi.org/10.1093/gigascience/giaa151.
984 60. McGinnis, C.S., Murrow, L.M., and Gartner, Z.J. (2019). DoubletFinder: Doublet
985 Detection in Single-Cell RNA Sequencing Data Using Artificial Nearest Neighbors. Cell
986 Syst. *8*, 329-337.e4. https://doi.org/10.1016/j.cels.2019.03.003.

61. Korsunsky, I., Millard, N., Fan, J., Slowikowski, K., Zhang, F., Wei, K., Baglaenko, Y., Brenner, M., Loh, P. ru, and Raychaudhuri, S. (2019). Fast, sensitive and accurate integration of single-cell data with Harmony. Nat. Methods *16*, 1289–1296. https://doi.org/10.1038/s41592-019-0619-0.
62. Reimand, J., Arak, T., Adler, P., Kolberg, L., Reisberg, S., Peterson, H., and Vilo, J. (2016). g:Profiler-a web server for functional interpretation of gene lists (2016 update). Nucleic Acids Res. *44*, W83–W89. https://doi.org/10.1093/NAR/GKW199.
63. Lopes, G., Bonacchi, N., Frazão, J., Neto, J.P., Atallah, B. V., Soares, S., Moreira, L., Matias, S., Itskov, P.M., Correia, P.A., et al. (2015). Bonsai: An event-based framework for processing and controlling data streams. Front. Neuroinform. *9*. https://doi.org/10.3389/fninf.2015.00007.
64. Mathis, A., Mamidanna, P., Cury, K.M., Abe, T., Murthy, V.N., Mathis, M.W., and Bethge, M. (2018). DeepLabCut: markerless pose estimation of user-defined body parts with deep learning. Nat. Neurosci. *21*, 1281–1289. https://doi.org/10.1038/s41593-018-0209-y.
65. Virtanen, P., Gommers, R., Oliphant, T.E., Haberland, M., Reddy, T., Cournapeau, D., Burovski, E., Peterson, P., Weckesser, W., Bright, J., et al. (2020). SciPy 1.0: fundamental algorithms for scientific computing in Python. Nat. Methods *17*, 261–272. https://doi.org/10.1038/s41592-019-0686-2.
66. Akam, T., Lustig, A., Rowland, J.M., Kapanaiah, S.K., Esteve-Agraz, J., Panniello, M., Márquez, C., Kohl, M.M., Kätzel, D., Costa, R.M., et al. Open-source, Python-based, hardware and software for controlling behavioural neuroscience experiments. https://doi.org/10.7554/eLife.
67. Berg, S., Kutra, D., Kroeger, T., Straehle, C.N., Kausler, B.X., Haubold, C., Schiegg, M., Ales, J., Beier, T., Rudy, M., et al. (2019). ilastik: interactive machine learning for (bio)image analysis. Nat. Methods *16*, 1226–1232. https://doi.org/10.1038/s41592-019-0582-9.
68. Klein, S., Staring, M., Murphy, K., Viergever, M.A., and Pluim, J.P.W. (2010). elastix: A Toolbox for Intensity-Based Medical Image Registration. IEEE Trans. Med. Imaging *29*, 196–205. https://doi.org/10.1109/TMI.2009.2035616.

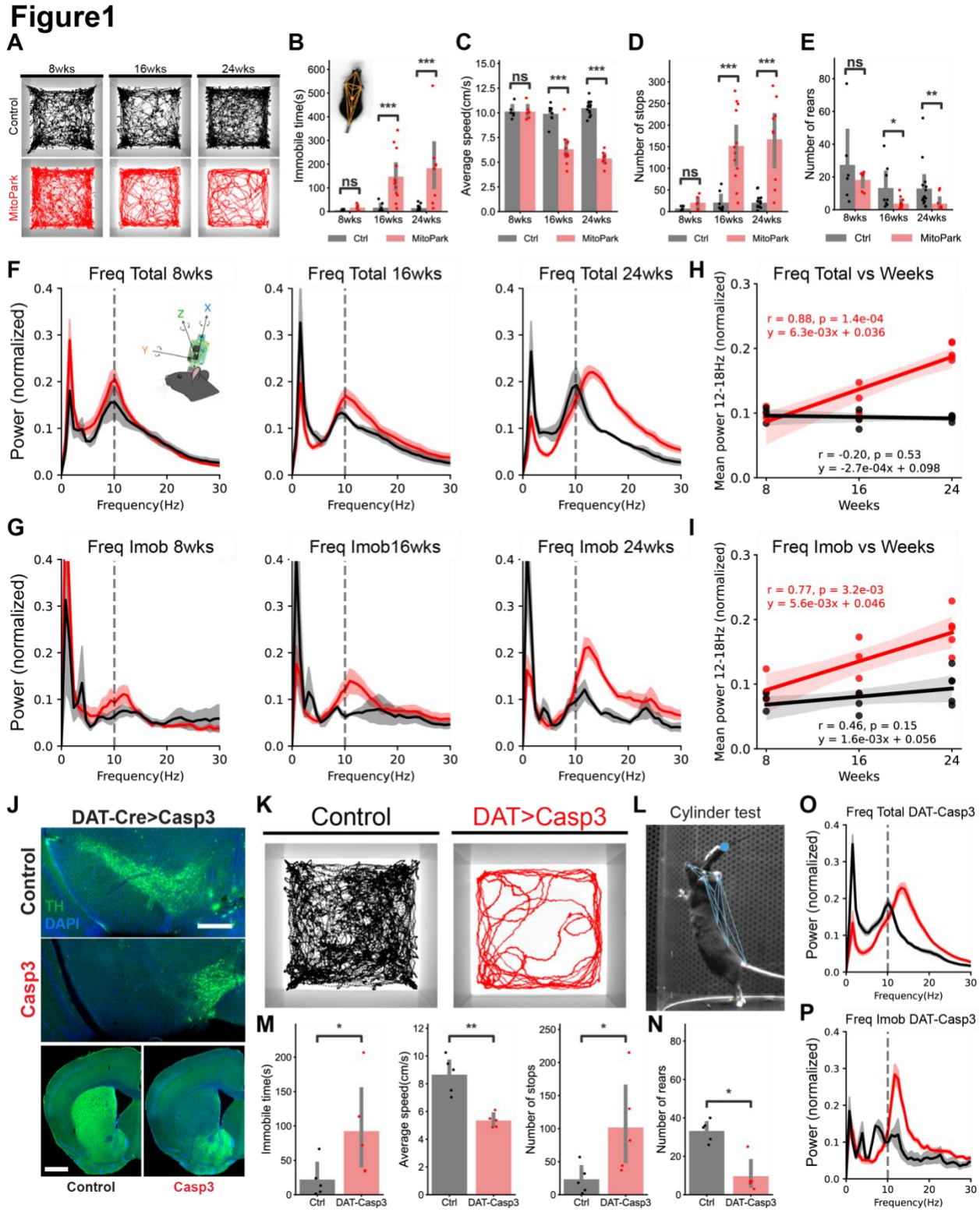

1017

1018 **Fig.1 Progressive development of PD-like motor deficits in MitoPark mice**

A. Cumulative trajectories of a representative MitoPark mouse and their control at different stages (8, 16 and 24wks) in the open-field test (black: control animals, red: MitoPark mice). **B-E**. Behavioral characterization of MitoPark mice and their littermate controls at each stage. **(B)** Immobility time: MitoPark mice at later stages spent significantly more time immobile compared to controls. The inset shows tracking performed using DeepLabCut. **(C)** Average speed during mobility: the speed of MitoPark mice was significantly lowered in 16 and 24wks. **(D)** Number of stops: the number of pauses in MitoPark mice showed significant differences compared to the controls. (**E**) Number of rears: MitoPark mice exhibited a significant reduction in rearing behavior at later stages. Statistical significance was determined by two-sided Mann–Whitney U-test (*$p < 0.05$, **$p < 0.01$, ***$p < 0.001$; ns = not statistically significant). Error bars show 95% confidence intervals. MitoPark 8weeks, n=6; Littermate controls 8weeks, n=6; MitoPark 16weeks, n=12; Littermate controls 16weeks, n=8; MitoPark 24weeks, n=9; Littermate controls 24weeks, n=15. **F-I.** Frequency analysis of total time **(F)** or immobility periods **(G)** at different ages of the animals. Mitopark mice showed a pronounced increase in the power of acceleration oscillations at the 12-18Hz range that becomes more prominent in the later stages. **(H, I)** The scatter plots show the correlation between age and mean power in the 12-18Hz frequency band for Mitopark mice and control animals during total period **(H)** or immobile period **(I)**. Pearson's correlation coefficient reveals a strong positive correlation during both the total period (H: red, $r=0.88$, $p<0.001$) and the immobile period (I: red, $r=0.77$, $p<0.01$) in MitoPark mice. The solid line represents the linear regression model (H: red, $y = 6.3e\text{-}03x + 0.036$, $R^2 = 0.78$; I: red, $y = 5.6e\text{-}03x + 0.036$, $R^2 = 0.60$), demonstrating a statistically significant relationship between the two variables in MitoPark mice. MitoPark 8weeks, n=3; Littermate controls 8weeks, n=3; MitoPark 16weeks, n=4; Littermate controls 16weeks, n=3; MitoPark 24weeks, n=5; Littermate controls 24weeks, n=6. **J-P.** Injections of Casp3 virus in the SNc of DAT-Cre mice led to the similar phenotype of MitoPark mice 24 weeks. **(J)** The images demonstrated a specific reduction in dopamine neurons (DANs) within the SNc, as confirmed by staining with anti-TH antibody (green). **(K-N)** The DAT-Casp3 animals showed motor deficits characterized by diminished movement speed, increased incidences of halting and reduced the frequency of rearing behaviors. Statistical significance was determined by two-sided Mann–Whitney U-test (*$p < 0.05$; ns = not statistically significant). Error bars show 95% confidence intervals. DAT-Casp3 animals, n=5; Controls, n=5. **(O, P)** The virus injection led to the presentation of the same 12-18Hz oscillation seen in MitoPark mice at 24 weeks.

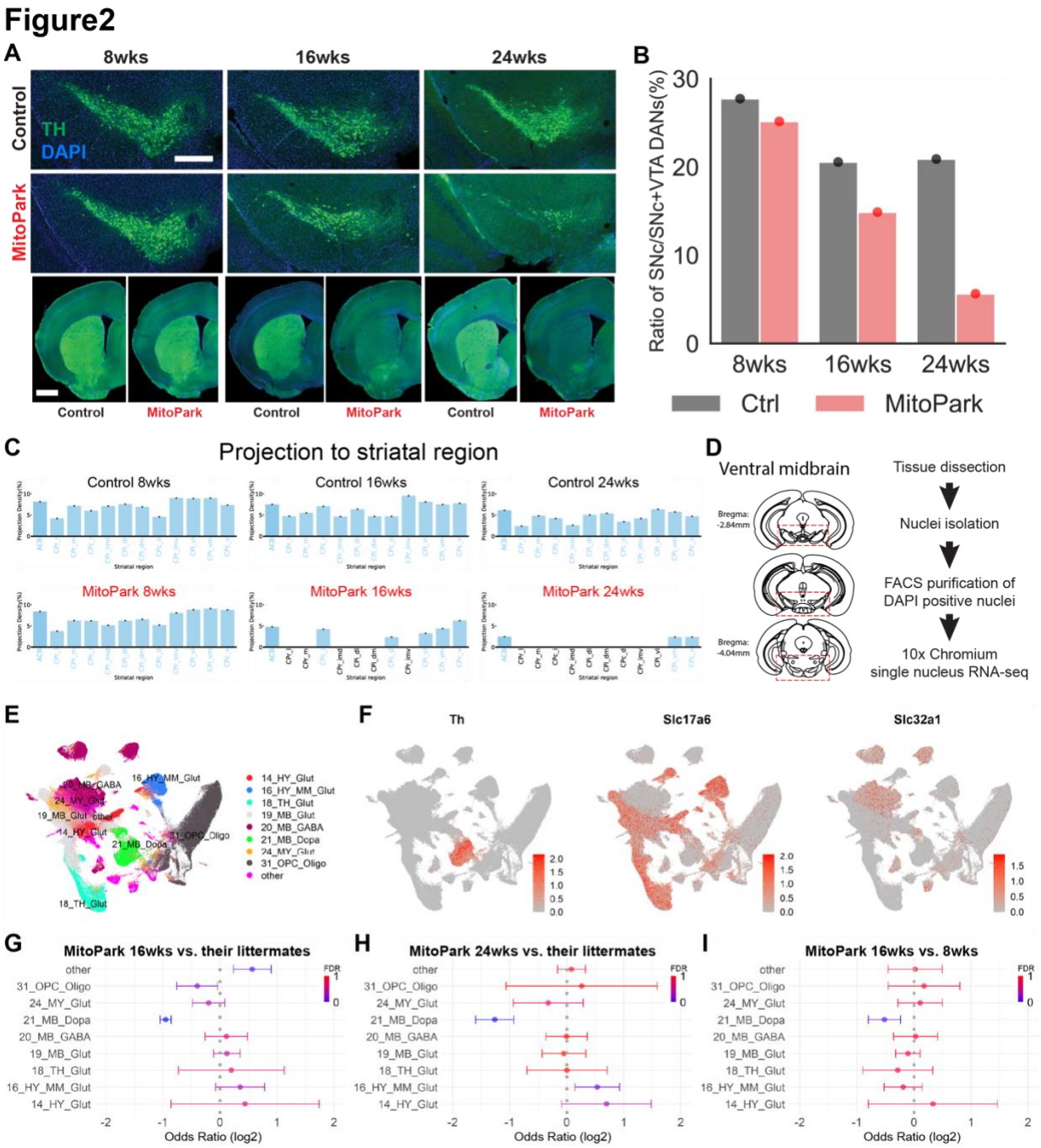

Fig.2 Progressive degeneration of dopamine neurons in MitoPark mice

A-C. TH immunohistochemistry of MitoPark mice and their littermate controls at 8, 16 and 24 weeks. (A) Histological images of the mice at each stage. Scale bars: 400μm for the substantia nigra (top) and 1mm for the striatum (bottom). (B-C) MitoPark mice exhibited a gradual and preferential loss of DANs in the substantia nigra, and their projections (each n=1). **D.** The workflow for single-nucleus RNA (snRNA) sequencing commenced with the collection of all tissues from the ventral midbrain (red dashed lines). The tissue samples underwent nuclei

1059 isolation, followed by the selection of DAPI+ nuclei. These nuclei were subsequently processed
1060 using the 10x Genomics platform for sequencing. **E.** UMAP visualization of snRNA-seq data
1061 from the ventral midbrain. Data are combined across all animals (MitoPark mice and their
1062 controls) and classified by the Allen Brain Cell (ABC) Atlas class annotations. Nuclei that are
1063 limited in number or belong to infrequent categories are designated as 'others.' **F.** Feature plot
1064 showing expression of marker genes used to label the main class of cells: *Th* (DANs), *Slc17a6*
1065 (excitatory neurons) and *Slc32a1* (inhibitory neurons). **G-I.** Dots and whiskers represent odds-
1066 ratio (OR) with 95% confidence interval (CI) obtained from MASC. OR estimates of major cell
1067 types associated with MitoPark mice (color; false discovery rate (FDR)-adjusted P<0.05). **(G)**
1068 MitoPark 16 weeks versus their littermate controls; 21_MB_Dopa (OR=-0.95, FDR-adjusted
1069 P<0.05). **(H)** MitoPark 24 weeks versus their littermate controls; 21_MB_Dopa (OR=-1.26, FDR-
1070 adjusted P<0.05). **(I)** MitoPark 16 weeks versus 8 weeks; 21_MB_Dopa (OR=-0.51, FDR-
1071 adjusted P=0.057).

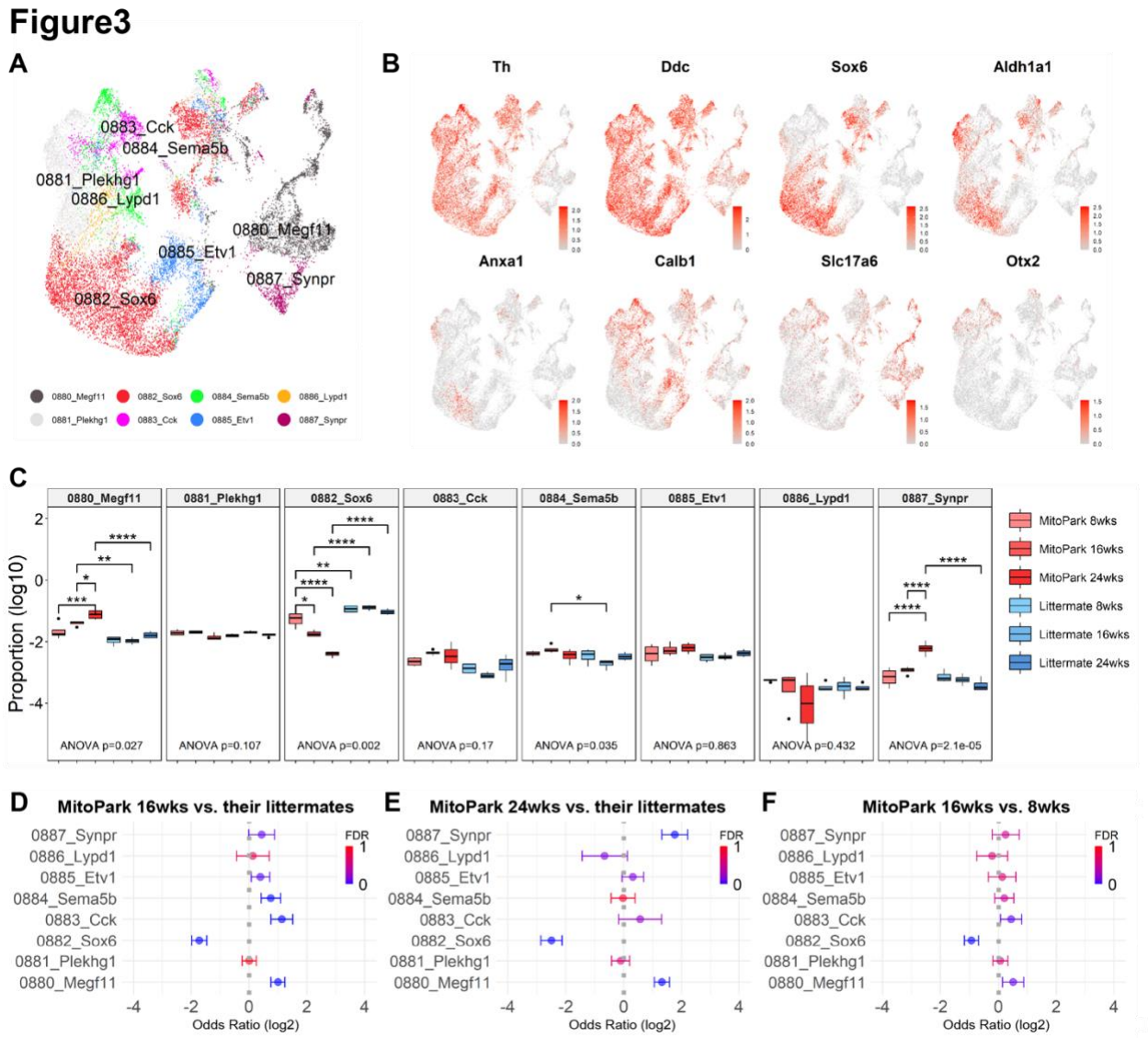

Fig.3 Subtype-specific degeneration within the dopaminergic populations

A. UMAP representation of 18,611 dopamine neuron nuclei, colored by the supertype annotation of the Allen Brain Cell (ABC) Atlas. In supertype annotation of the ABC Atlas, DANs are largely classified into 8 types. **B.** Representative feature plots showing gene expression associated with dopamine used to label the main class of cells. **C.** Distribution of dopamine subtype proportions across MitoPark and their control animals. 0882_Sox6 is mostly affected among other dopamine neuron subtypes. Statistical significance was determined by two-way ANOVA (p-value indicates the interaction effect between genotype and age) followed by Tukey's HSD test for multiple comparisons (*p < 0.05, **p < 0.01, ***p < 0.001, ****p < 0.0001). **D-F.** Odds-ratio estimates of each dopamine subpopulation in **(D)** MitoPark 16 weeks versus their littermate controls; 0882_Sox6 (OR=-1.72, FDR-adjusted P<0.05), 0880_Megf11

1084 (OR=1.00, FDR-adjusted P<0.05) and 0883_Cck (OR=1.13, FDR-adjusted P<0.05). **(E)**
1085 MitoPark 24 weeks versus their littermate controls; 0882_Sox6 (OR=-2.49, FDR-adjusted
1086 P<0.05), 0887_Synpr (OR=1.76, FDR-adjusted P<0.05) and 0880_Megf11 (OR=1.31, FDR-
1087 adjusted P<0.05). **(F)** MitoPark 16 weeks versus 8 weeks; 0882_Sox6 (OR=-0.93, FDR-
1088 adjusted P=0.057).

Figure4

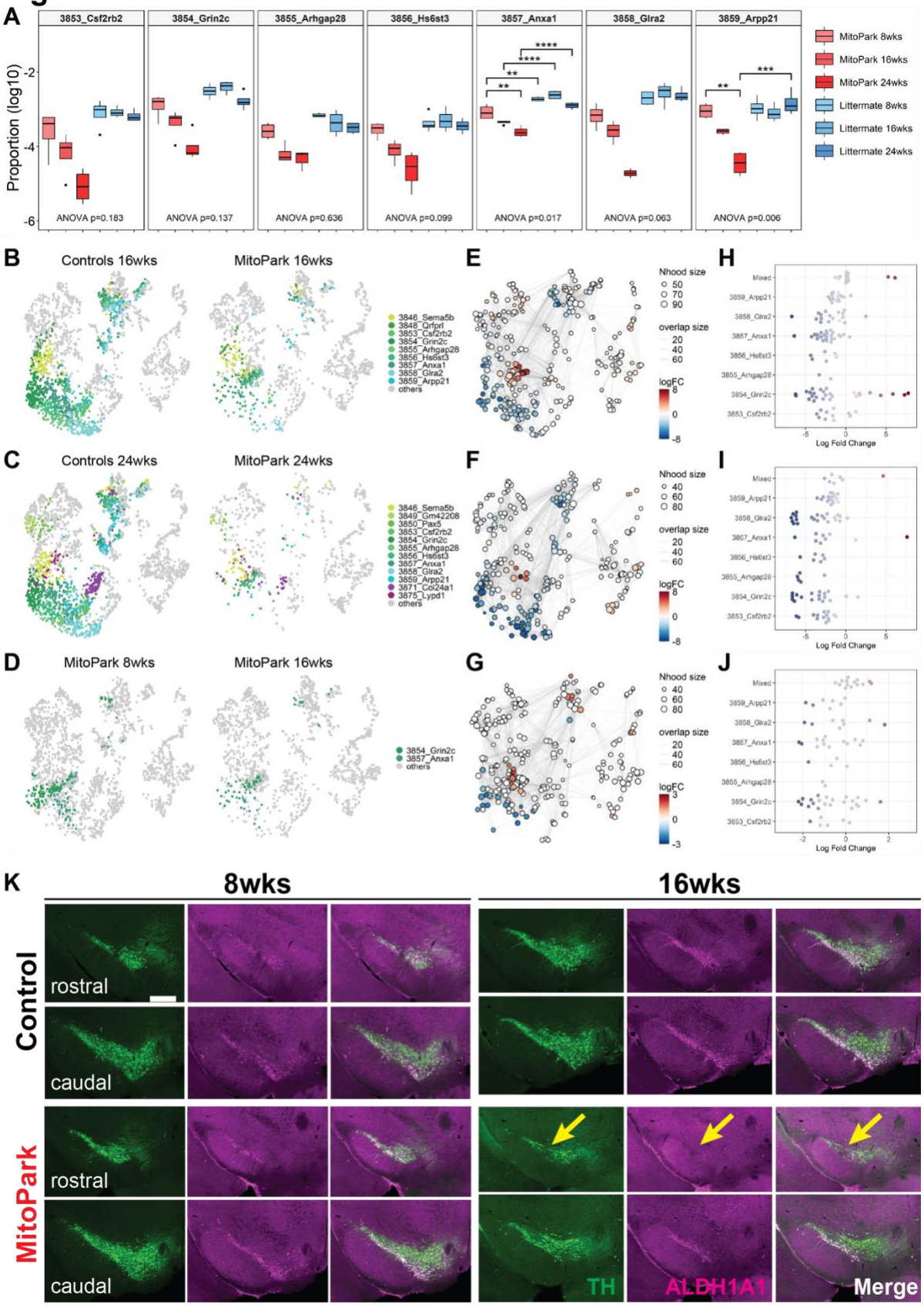

1089

1090 **Fig.4 A subset of *Sox6+* population is more vulnerable than others in MitoPark mice**
1091 Differential abundance analysis for the dopamine clusters of MitoPark mice and their littermate
1092 controls. The analysis reveals a subtype-specific reduction in MitoPark mice at a later stage.
1093 **A.** Distribution of *Sox6+* dopamine subtype proportions across MitoPark and their control
1094 animals. 3857_Anxa1 is significantly affected among other dopamine neuron subtypes at 16
1095 and 24 weeks. Statistical significance was determined by two-way ANOVA (p-value indicates
1096 the interaction effect between genotype and age) followed by Tukey's HSD test for multiple
1097 comparisons (*$p < 0.05$, **$p < 0.01$, ***$p < 0.001$, ****$p < 0.0001$). **B-D.** UMAP plots illustrating
1098 dopamine neuron subpopulations in MitoPark mice and their littermate controls (n = 8 per
1099 genotype and stage), highlighting clusters with significant differential abundance (log fold
1100 change < 2). The gene groups affected across all comparisons are shown: (B) Controls vs.
1101 MitoPark at 16 weeks, (C) Controls vs. MitoPark at 24 weeks, and (D) MitoPark at 8 vs. 16
1102 weeks, as identified by the differential abundance analysis. **E-G.** Neighborhood (Nhood) graphs
1103 with the results from Milo differential abundance testing between MitoPark mice and controls
1104 (E:16 weeks, F: 24 weeks), and between MitoPark mice at different stages (G: 8 and 16 weeks).
1105 Nodes represent neighborhoods, colored by their log fold change compared to their controls
1106 (blue: less abundant, red: more abundant, gray: non-differentially abundant). Graph edges show
1107 the number of cells shared between two neighborhoods. **H-J**. Beeswarm plots display the
1108 distribution of log-fold changes in cell abundance. Dots representing neighborhoods that overlap
1109 with the same cell populations are grouped together. Colors are represented similarly to **E-G**. **K.**
1110 Histological images representing 8 and 16 weeks of MitoPark mice reveal that significant cell
1111 depletion in the ventral region, particularly in the rostral part of the SNc (TH: green, ALDH1A1:
1112 magenta). Scale bar 400μm.

Figure5

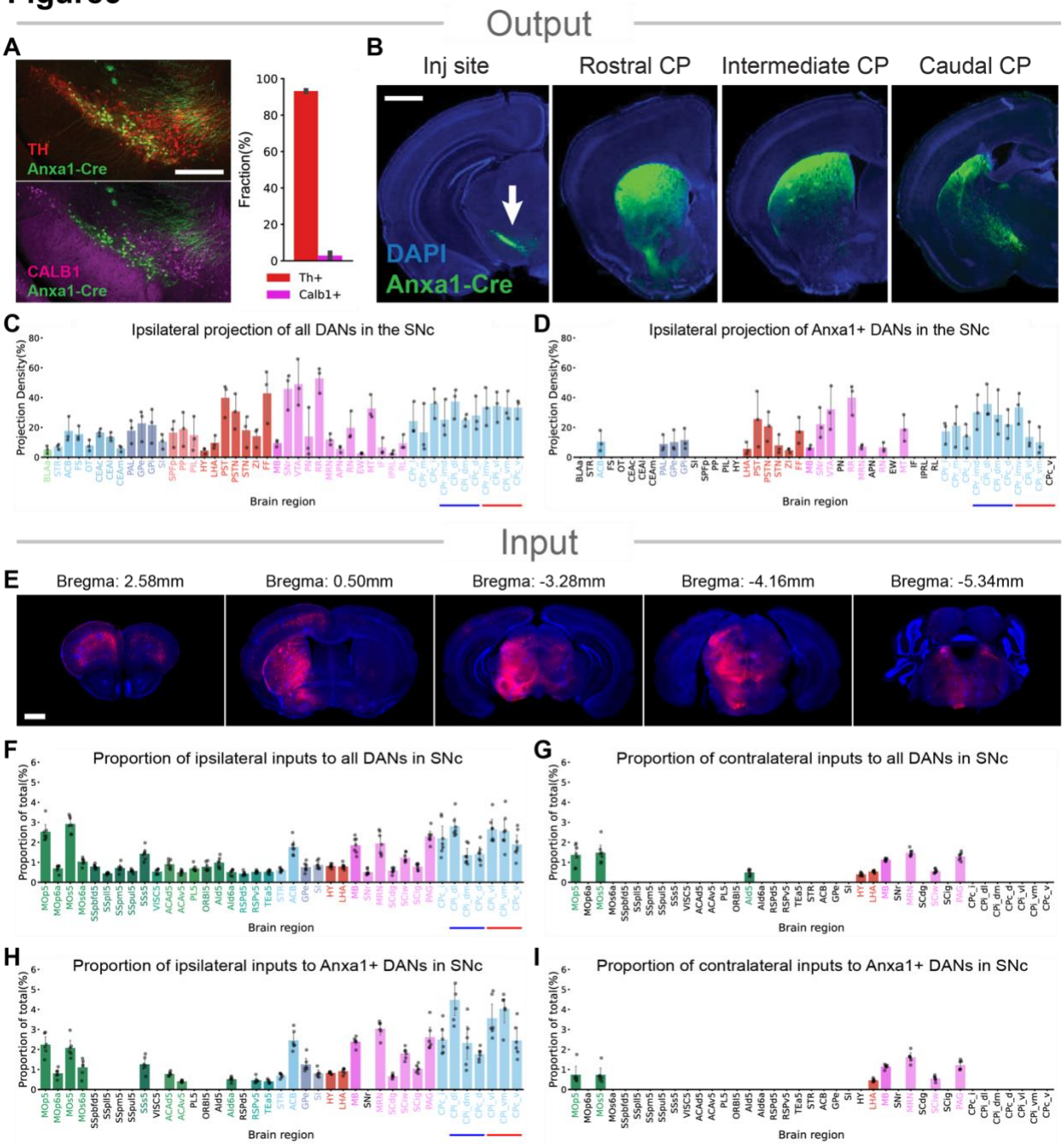

Fig.5 Input-output circuit architecture of *Anxa1*+ DANs in the SNc

A. In the Anxa1-Cre line, the majority of neurons within the SNc are positive for *Th* and negative for *Calbindin1* (TH, red; CALB1, magenta; n=2). Scale bars: 400μm. **B.** Axonal projections of *Anxa1*+ DANs in the SNc. They preferentially project to dorsal striatum that integrates sensorimotor information from cortical and thalamic regions. Scale bars: 1mm. **C-D.** Brain regions to which all DANs or *Anxa1*+ DANs in the SNc project, measured as the fraction

1120 of neurites found within those brain structures defined Allen brain atlas (each n=3). Blue
1121 horizontal line indicates dorsal striatum and the red line indicates ventral striatum. **E.**
1122 Representative images of rabies infected cells (tdTomato). Rabies virus was injected in the SNc
1123 of Anxa1-Cre counterstained with DAPI in blue. Scale bar 1mm. **F-I.** Statistical analysis of the
1124 whole-brain distribution of ipsilateral (left) or contralateral (right) monosynaptic inputs to all
1125 DANs (F, G) or *Anxa1+* dopamine neuron subtype (H, I) in the SNc. Average proportion of
1126 tdTomato-labeled neurons in approximately 50 brain regions, each with more than 200 cells,
1127 was greater than 0.2% of the total input to DANs in DAT-Cre mice (n=7) and Anxa1-Cre mice
1128 (n=5; 4 animals for Anxa1-Cre+ and 1 animal for DAT-Flp+;Anxa1-Cre+). Brain areas are color-
1129 coded by the Allen Brain Atlas.
1130 **[Acronym]** ACAd5, Anterior cingulate area, dorsal part, layer 5; ACAv5, Anterior cingulate area,
1131 ventral part, layer 5; ACB, Nucleus accumbens; AId5, Agranular insular area, dorsal part, layer
1132 5; AId6a, Agranular insular area, dorsal part, layer 6a; APN, Anterior pretectal nucleus; BLAa,
1133 Basolateral amygdalar nucleus, anterior part; CEAc, Central amygdalar nucleus, capsular part;
1134 CEAl, Central amygdalar nucleus, lateral part; CEAm, Central amygdalar nucleus, medial part;
1135 CPc_d, Caudal Caudoputamen, dorsal; CPc_i, Caudal Caudoputamen, intermediate; CPc_v,
1136 Caudal Caudoputamen, ventral; CPi_dl, Intermediate Caudoputamen, dorsolateral; CPi_dm,
1137 Intermediate Caudoputamen, dorsomedial; CPi_vl, Intermediate Caudoputamen, ventrolateral;
1138 CPi_vm, Intermediate Caudoputamen, ventromedial; CPr_imd, Rostral Caudoputamen,
1139 intermediate dorsal; CPr_imv, Rostral Caudoputamen, intermediate ventral; CPr_l, Rostral
1140 Caudoputamen, lateral; CPr_m, Rostral Caudoputamen, medial; EW, EdingerWestphal nucleus;
1141 FF, Fields of Forel; FS, Fundus of striatum; Gpe, Globus pallidus, external segment; Gpi,
1142 Globus pallidus, internal segment; HY, Hypothalamus; IF, Interfascicular nucleus raphe; IPRL,
1143 Interpeduncular nucleus, rostrolateral; LHA, Lateral hypothalamic area; MB, Midbrain; MOp5,
1144 Primary motor area, Layer 5; MOp6a, Primary motor area, Layer 6a; MOs5, Secondary motor
1145 area, layer 5; MOs6a, Secondary motor area, layer 6a; MRN, Midbrain reticular nucleus; MT,
1146 Medial terminal nucleus of the accessory optic tract; ORBl5, Orbital area, lateral part, layer 5;
1147 OT, Olfactory tubercle; PAG, Periaqueductal gray; PAL, Pallidum; PIL, Posterior intralaminar
1148 thalamic nucleus; PL5, Prelimbic area, layer 5; PN, Paranigral nucleus; PP, Peripeduncular
1149 nucleus; PST, Preparasubthalamic nucleus; PSTN, Parasubthalamic nucleus; RL, Rostral linear
1150 nucleus raphe; RN, Red nucleus; RR, Midbrain reticular nucleus, retrorubral area; RSPd5,
1151 Retrosplenial area, dorsal part, layer 5; RSPv5, Retrosplenial area, ventral part, layer 5; SCdg,
1152 Superior colliculus, motor related, deep gray layer; Scig, Superior colliculus, motor related,
1153 intermediate gray layer; Sciw, Superior colliculus, motor related, intermediate white layer; SI,

Substantia innominata; SNr, Substantia nigra, reticular part; SPFp, Subparafascicular nucleus, parvicellular part; SSpbfd5, Primary somatosensory area, barrel field, layer 5; SSpll5, Primary somatosensory area, lower limb, layer 5; SSpm5, Primary somatosensory area, mouth, layer 5; SSpul5, Primary somatosensory area, upper limb, layer 5; SSs5, Supplemental somatosensory area, layer 5; STN, Subthalamic nucleus; STR, Striatum; TEa5, Temporal association areas, layer 5; VISC5, Visceral area, layer 5; VTA, Ventral tegmental area; ZI, Zona incerta

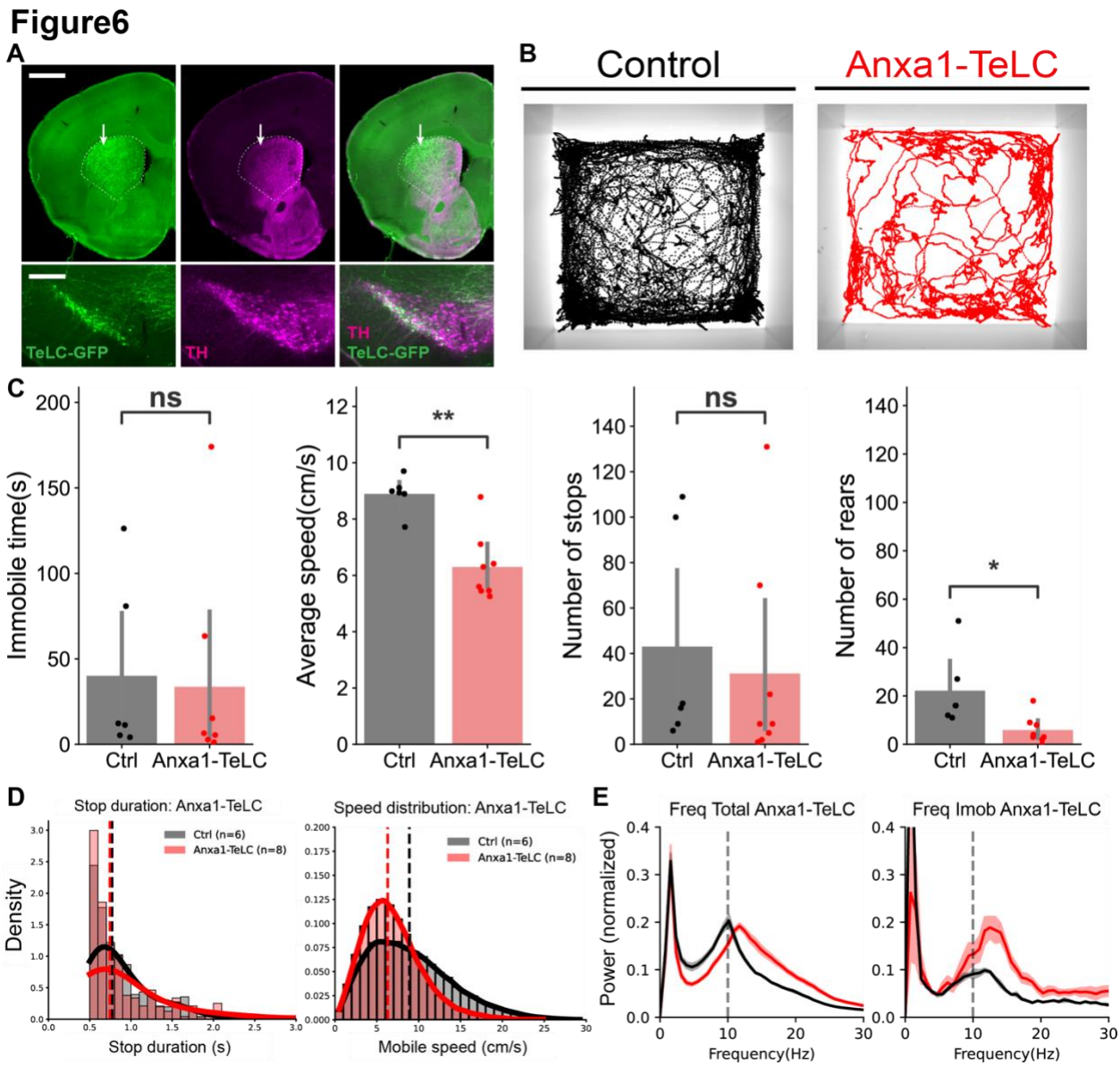

Fig.6 Inhibition of *Anxa1*+ DANs leads to motor deficits resembling early onset PD-like symptoms

A. In the Anxa1-Cre line, targeted expression of the tetanus toxin light chain (TeLC) specifically eliminated dopamine synaptic transmission in the dorsal striatum (white arrows). Scale bars: 1mm for the striatum (top) and 400μm for the substantia nigra (bottom). **B-D.** Behavioral characterization of Anxa1-TeLC animals. (B) Cumulative trajectories of a representative Anxa1-TeLC mouse and their control in the open-field test (black: a control animal, red: Anxa1-TeLC mouse). (C) Anxa1-TeLC animals demonstrated slowed movement; however, there were no significant differences observed in terms of immobility duration or the frequency of stops. The frequency of rearing behaviors in the Anxa1-TeLC animals was significantly reduced. Statistical

1171 significance was determined by two-sided Mann–Whitney U-test (**$p < 0.01$, *$p < 0.05$; ns = not
1172 statistically significant). Error bars show 95% confidence intervals. Anxa1-TeLC animals, n=5;
1173 Controls, n=4. (D) This figure shows the probability density function (PDF) for stop duration (left)
1174 and speed distribution (right), with duration (in seconds) or speed (cm/s) on the x-axis and
1175 probability density on the y-axis. There is no significant difference in the distribution of stop
1176 durations between Anxa1-TeLC and control animals, although the speed distribution in Anxa1-
1177 TeLC animals is slightly shifted to the left, indicating slower movement. **E.** Anxa1-TeLC animals
1178 showed the similar 12-18Hz oscillation seen in MitoPark mice at 16 weeks.

Extended Data Fig.1

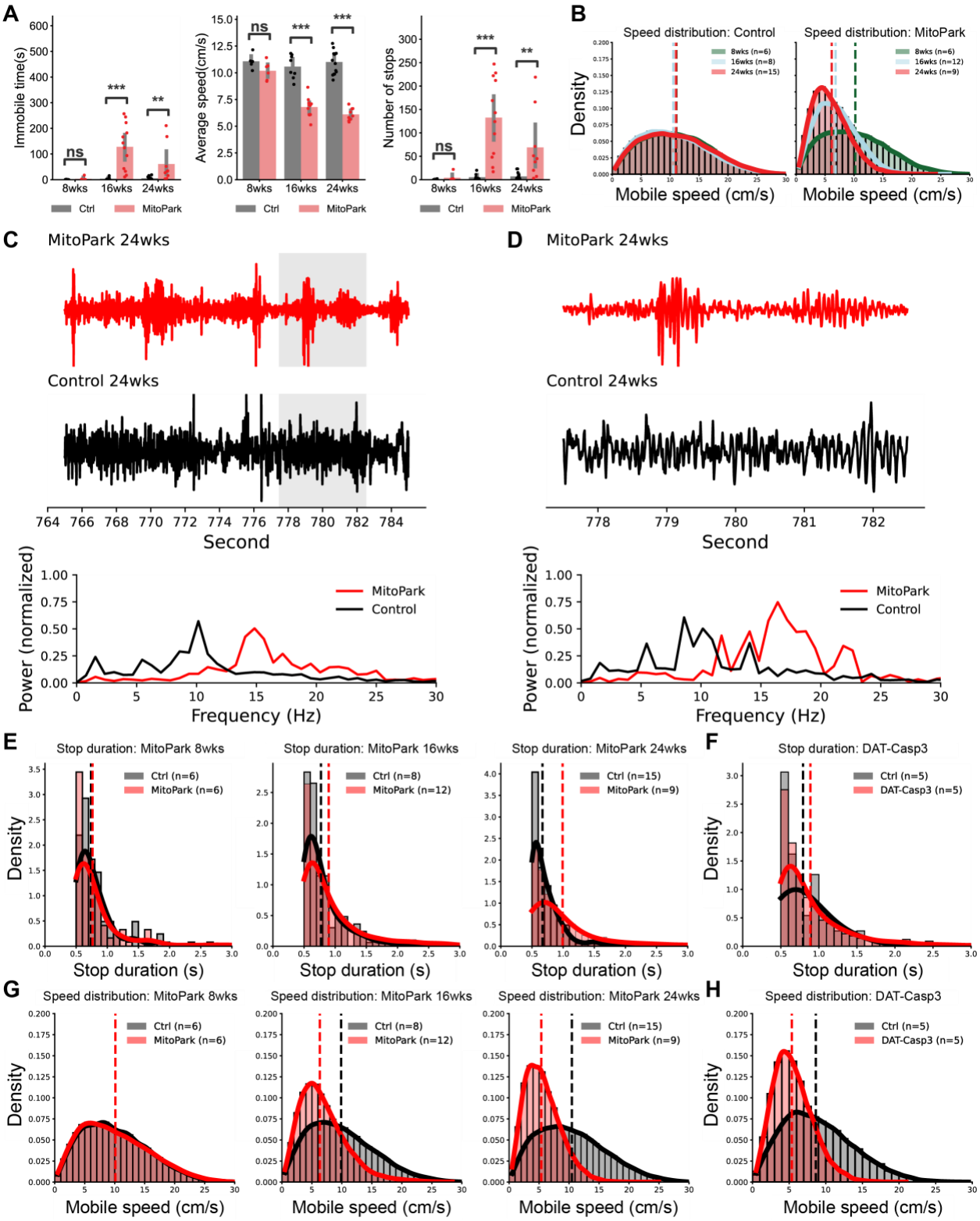

Extended Data Fig.1 Behavioral changes associated with the progression of neurodegeneration in MitoPark mice, Related to Fig.1

1182 **A-B.** Environmental novelty does not influence basic locomotor activity in MitoPark animals.
1183 Measures of immobility time, average speed, and number of stops on the initial habituation
1184 day (Day 0) did not differ significantly from those recorded on the actual testing day (Day 1).
1185 Although average speed was slightly higher on Day 0, this likely reflects heightened
1186 exploratory drive and motivation in response to the novel environment (A). Similarly, speed
1187 distribution analysis showed no significant differences between the two days (B). **C-D.**
1188 Examples of raw traces of dynamic acceleration in MitoPark animal 24 weeks (red) and a
1189 control animal (black), with an enlarged view (gray square in A) shown in **C**. MitoPark mice often
1190 show specific 12-18Hz oscillations. **E-H.** These figures show the probability density functions
1191 (PDFs) for stop duration and speed, with duration (s) and speed (cm/s) on the x-axis and
1192 probability density on the y-axis. In MitoPark mice, stop durations increased and speed
1193 distributions shifted leftward at later stages (E, G). DAT-Casp3 animals exhibited a similar
1194 pattern, with prolonged stop durations and reduced speeds (F, H), resembling the later-stage
1195 phenotype of MitoPark mice.

Extended Data Fig.2

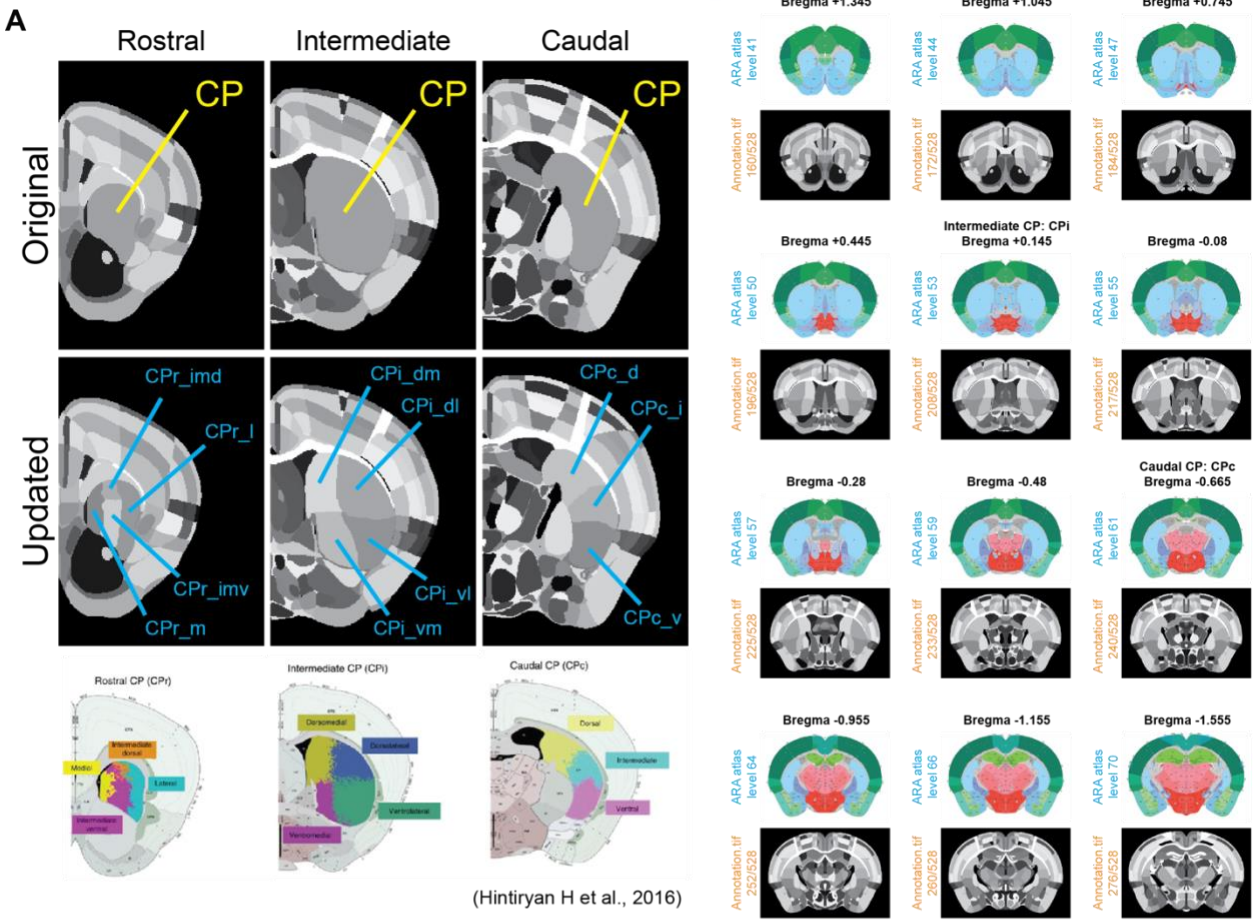

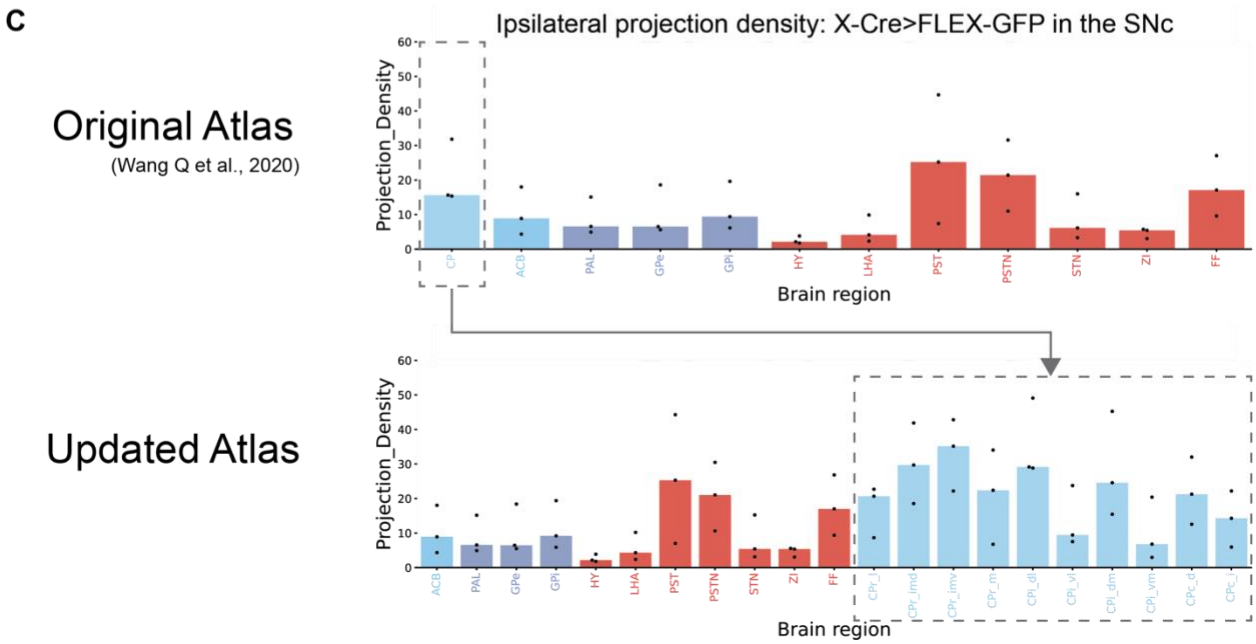

1196

Extended Data Fig.2 An updated atlas incorporates striatal subregions and enhances the analysis of cells and projections, Related to Fig.2 and Fig.5

A. Top: The original Allen Common Coordinate Framework (Allen CCF; version 3 released in 2017). Middle: An updated version of the Allen CCF, incorporating subregions of the striatum (CP: caudate putamen) based on the cortical projections shown at the bottom (CPr_imd: Rostral CP – Intermediate dorsal, CPr_l: Rostral CP – Lateral, CPr_imv: Rostral CP – Intermediate ventral, CPr_m: Rostral CP – Medial, CPi_dm: Intermediate CP – Dorsomedial, CPi_dl: Intermediate CP – Dorsolateral, CPi_vl: Intermediate CP – Ventrolateral, CPi_vm: Intermeidiate CP – Ventromedial, CPc_d: Caudal CP – Dorsal, CPc_i: Caudal CP – Intermediate, CPc_v: Caudal CP – Ventral). **B.** Alignment of coordinates between the ABA (Allen Brain Atlas) and Allen CCFv3, with manually segmented subregions of the striatum. **C.** Comparison of projection density of dopamine neurons in SNc using the original atlas versus the updated atlas. The original atlas (top) does not include subdivisions of the caudate-putamen (CP), while the updated atlas (bottom) defines 11 subregions based on cortical projections, providing a more detailed representation of local projections within the striatum.

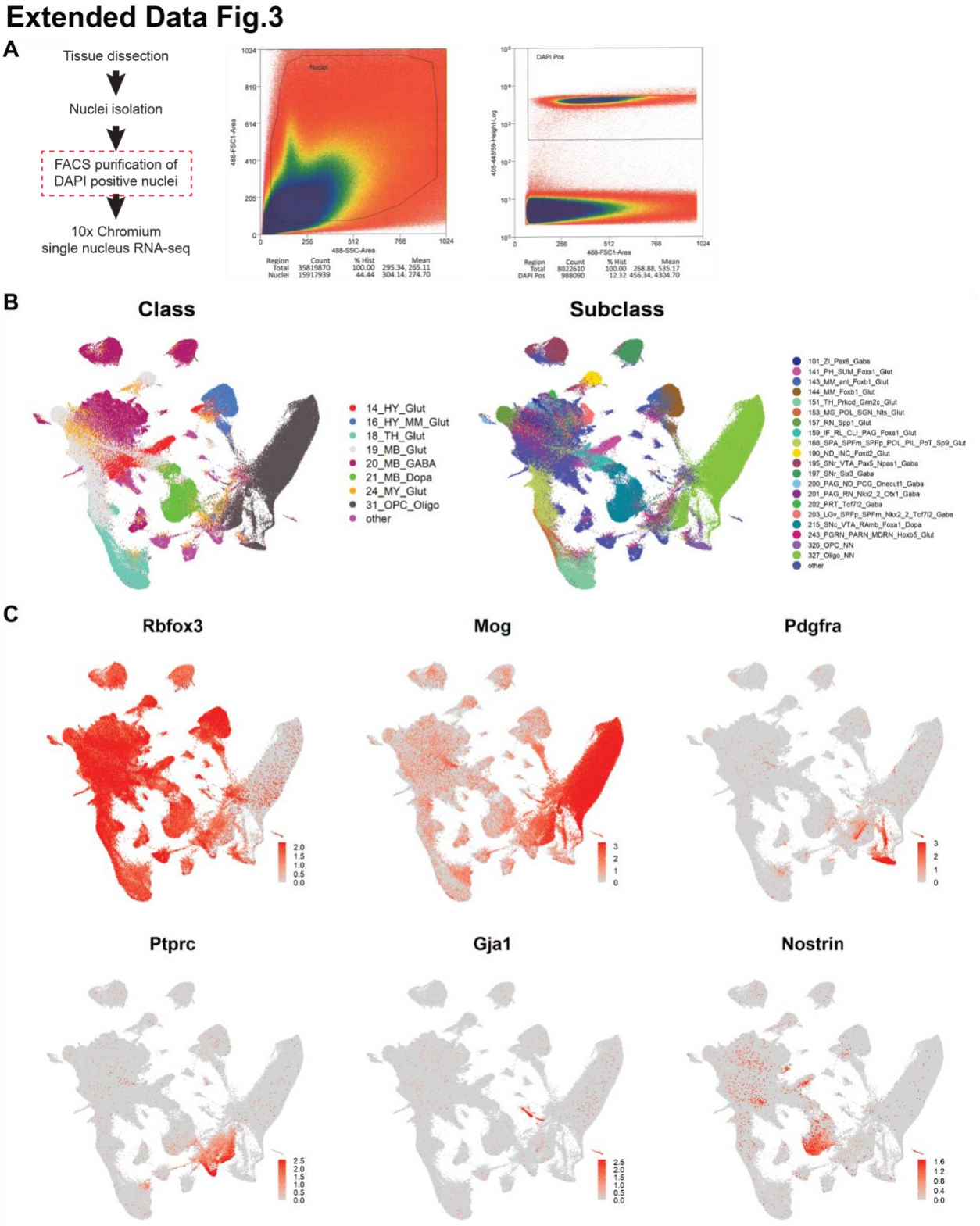

Extended Data Fig.3 The integrated dataset with the Allen Brain Cell (ABC) Atlas, Related to Fig.2

1215 **A.** UMAP plots showing all nuclei in the ventral midbrain of MitoPark mice and their controls with
1216 the class (left) or subclass (right) annotation of the ABC Atlas. Dopamine cluster is classified as
1217 Class: 21_MB_Dopa or Subclass: 215_SNc_VTA_RAmb_Foxa1_Dopa. **B.** Representative
1218 feature plots to label main class of cells. Neuronal cells, *Rbfox3*; Oligodendrocytes, *Mog*;
1219 Oligodendrocyte precursor cells (OPCs), *Pdgfra*; Microglia, *Ptprc*; Astrocytes, *Gja*; Endothelial
1220 cells, *Nostrin*.

Extended Data Fig.4

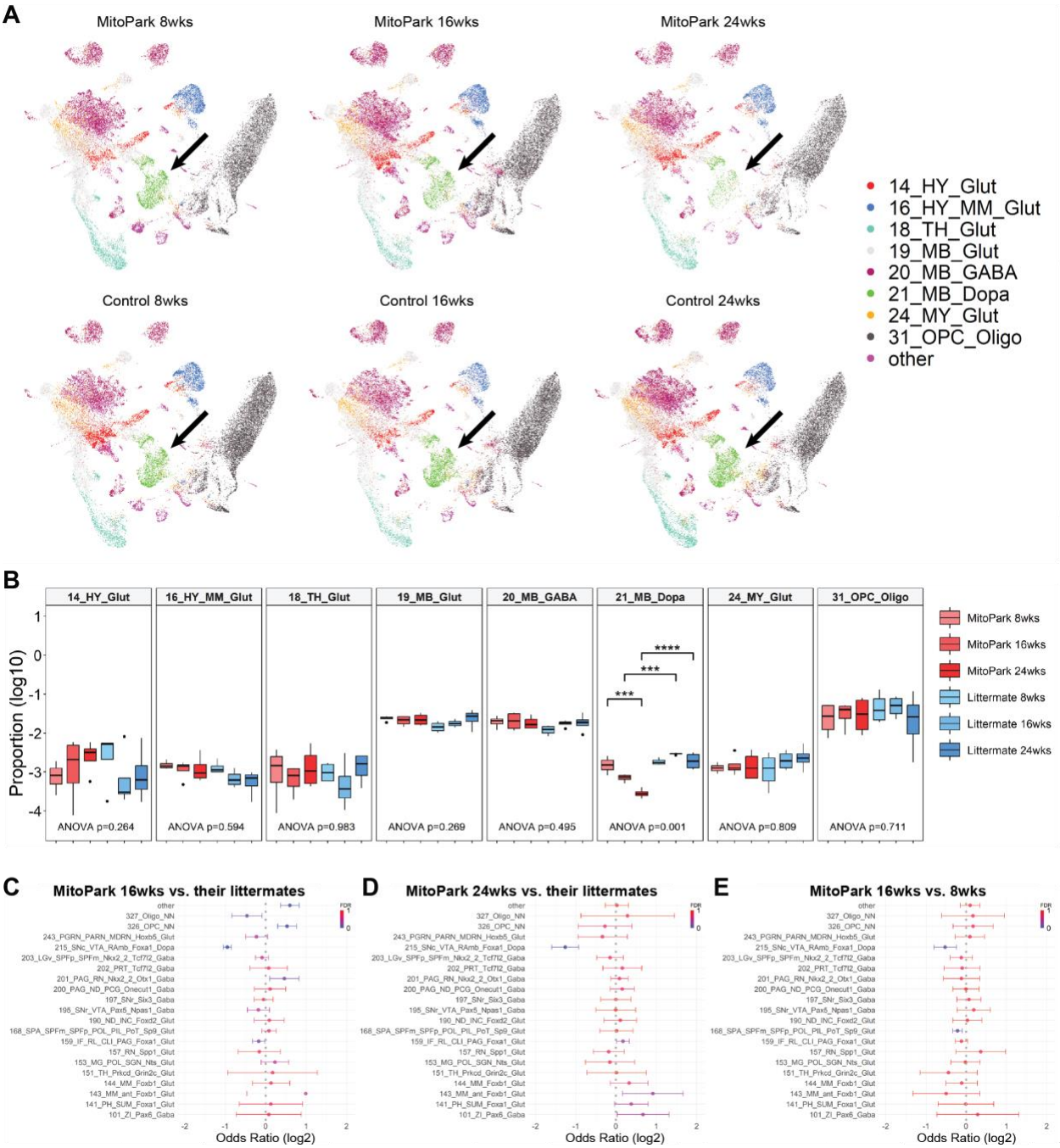

Extended Data Fig.4 A significant reduction in DANs was observed in the later weeks of MitoPark mice, Related to Fig.2

A. UMAP plots showing all nuclei in the ventral midbrain of MitoPark mice and their controls with the class annotation of the ABC Atlas. Dopamine cluster (black arrow) becomes visibly thinner than other cell types in MitoPark mice. **B.** Box and whisker plots showing the fraction of major cell types originating from the ventral midbrain of MitoPark mice, their littermate controls and B6

1228 WT mice (each n=8), with plot center, box and whiskers corresponding to median, interquartile
1229 range (IQR) and 1.5xIQR, respectively. MitoPark mice in the later stages exhibited a significant
1230 reduction in the proportion of DANs (21_MB_Dopa), without affecting other cell types. Statistical
1231 significance was determined by two-way ANOVA (p-value indicates the interaction effect
1232 between genotype and age) followed by Tukey's HSD test for multiple comparisons (*$p < 0.05$,
1233 **$p < 0.01$, ***$p < 0.001$, ****$p < 0.0001$). **C-E.** Odds-ratio estimated of major cell types
1234 annotated by subclass. **(C)** MitoPark 16 weeks versus their littermate controls;
1235 215_SNc_VTA_RAmb_Foxa1_Dopa (OR=-0.95, FDR-adjusted $P<0.05$). **(D)** MitoPark 24 weeks
1236 versus their littermate controls; 215_SNc_VTA_RAmb_Foxa1_Dopa (OR=-1.26, FDR-adjusted
1237 $P<0.05$). **(E)** MitoPark 16 weeks versus 8 weeks; 215_SNc_VTA_RAmb_Foxa1_Dopa (OR=-
1238 0.51, FDR-adjusted $P=0.086$).

Extended Data Fig.5

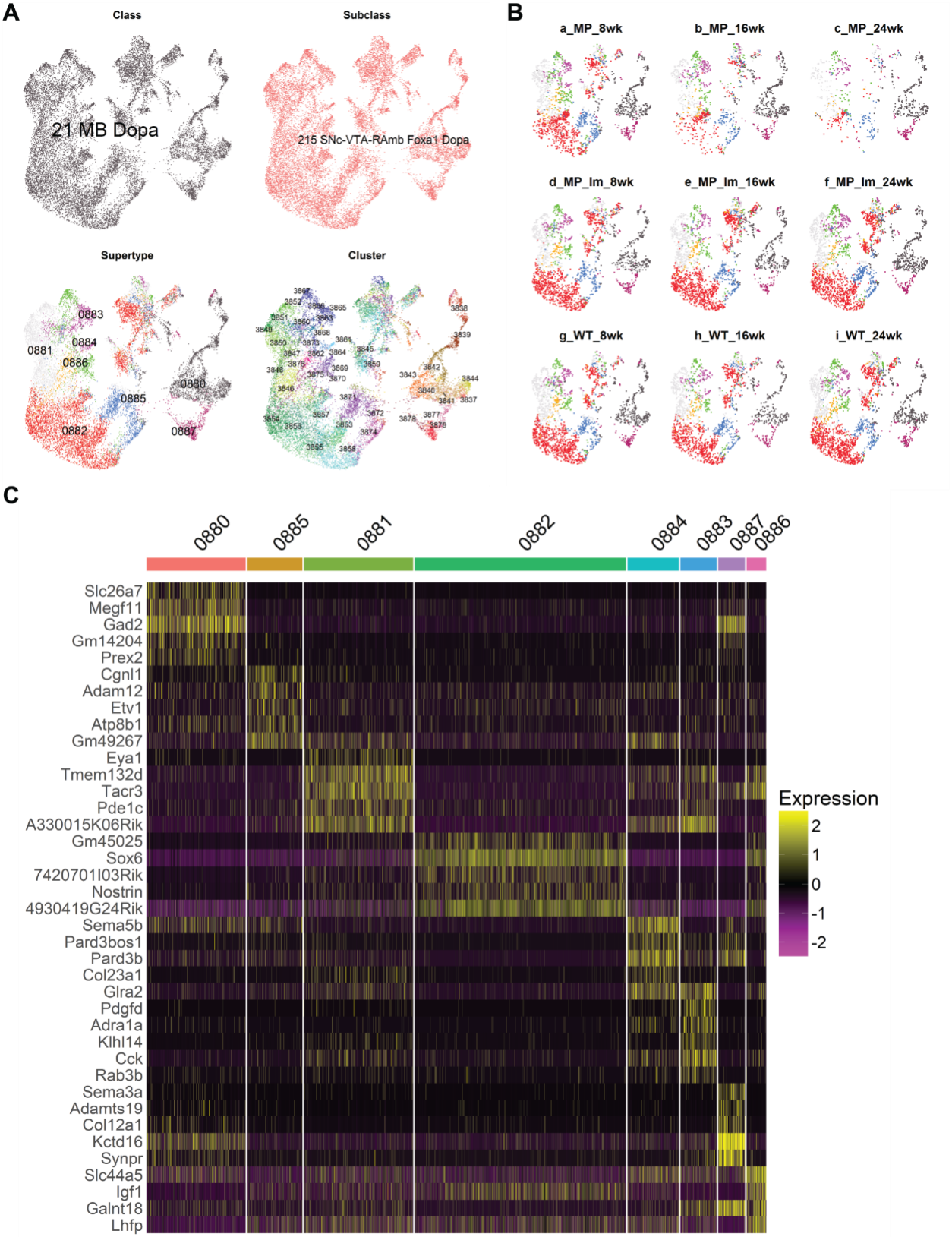

1239

1240 **Extended Data Fig.5 The dopaminergic cluster with distinct marker genes, Related to**
1241 **Fig.3**
1242 **A.** UMAP plots showing dopamine nuclei in the MitoPark mice and their controls with the
1243 annotations (Class, Subclass, Supertype and Cluster) of the ABC Atlas. **B.** UMAP plots
1244 illustrating the distribution of dopamine nuclei, categorized by supertype annotation based on
1245 the species and age. **C.** Top five marker genes for each dopamine neuron subtype categorized
1246 by supertype annotation.

Extended Data Fig.6

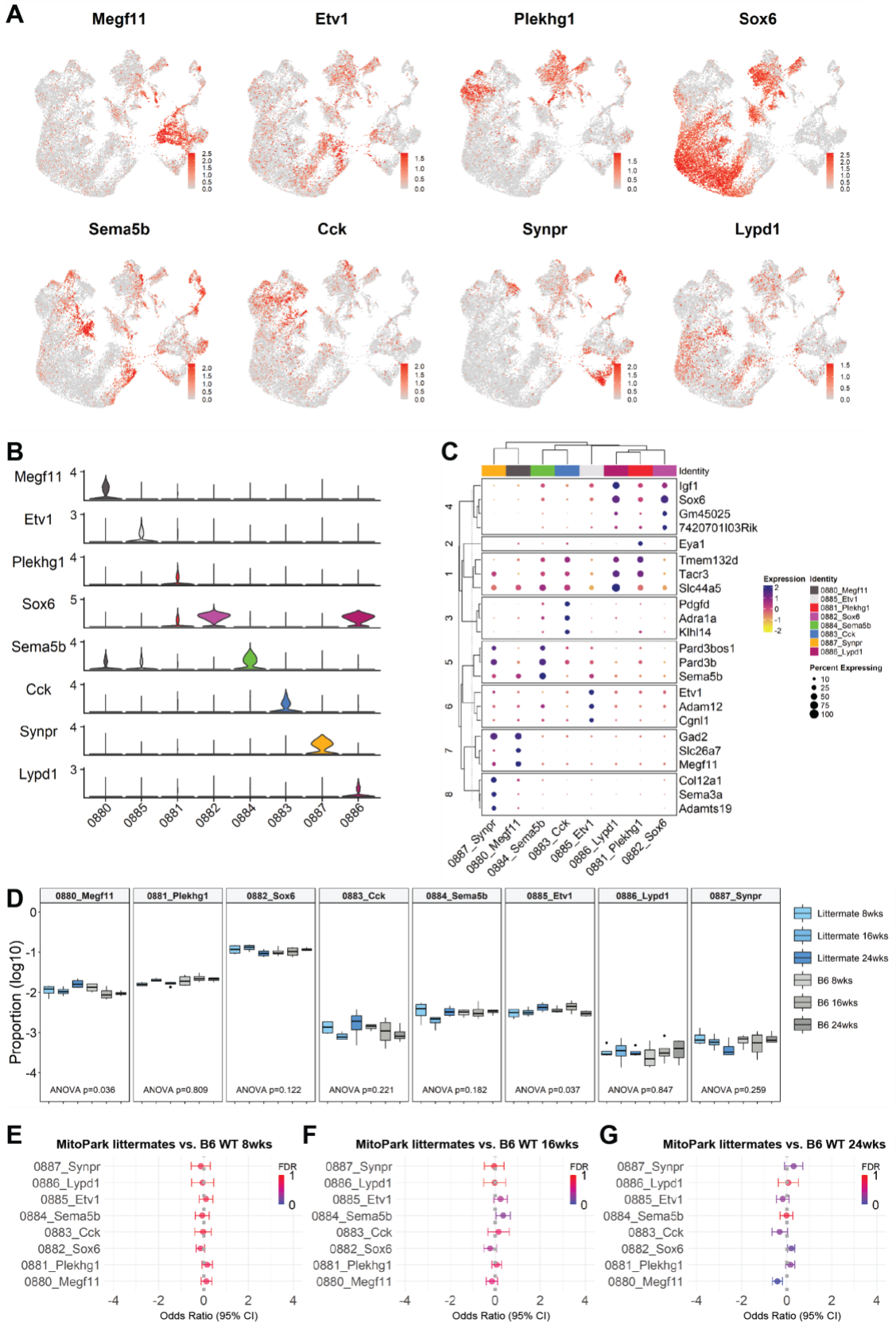

1247

1248 **Extended Data Fig.6 Marker feature expression in the dopaminergic cluster, Related to**
1249 **Fig.3**
1250 **A.** Feature plots depicting the expression of marker genes across dopamine clusters, classified
1251 according to supertype annotations.**B.** Violin plot indicating the expression distribution of the top
1252 marker gene of each cluster. **C.** Clustered dot plot profiling of marker genes for each dopamine
1253 cluster. X-axis represents the dopamine clusters, and the Y-axis shows the top three marker
1254 genes. Dot diameter indicates the proportion of cluster nuclei expressing a given gene. The
1255 color scale represents the gene expression levels, with black indicating high expression and
1256 white indicating low expression. **D.** Distribution of dopamine subtype proportions across
1257 MitoPark littermate control animals and B6 WT animals. **E-G.** There is no significant age-related
1258 degeneration in dopamine populations. **(E)** MitoPark littermate controls versus B6 WT animals
1259 at 8 weeks; 0882_Sox6 (OR=-0.14, FDR-adjusted P=0.80). **(E)** MitoPark littermate controls
1260 versus B6 WT animals at 16 weeks; 0882_Sox6 (OR=-0.21, FDR-adjusted P<0.41). **(F)**
1261 MitoPark littermate controls versus B6 WT animals at 24 weeks; 0882_Sox6 (OR=0.20, FDR-
1262 adjusted P<0.11).

Extended Data Fig.7

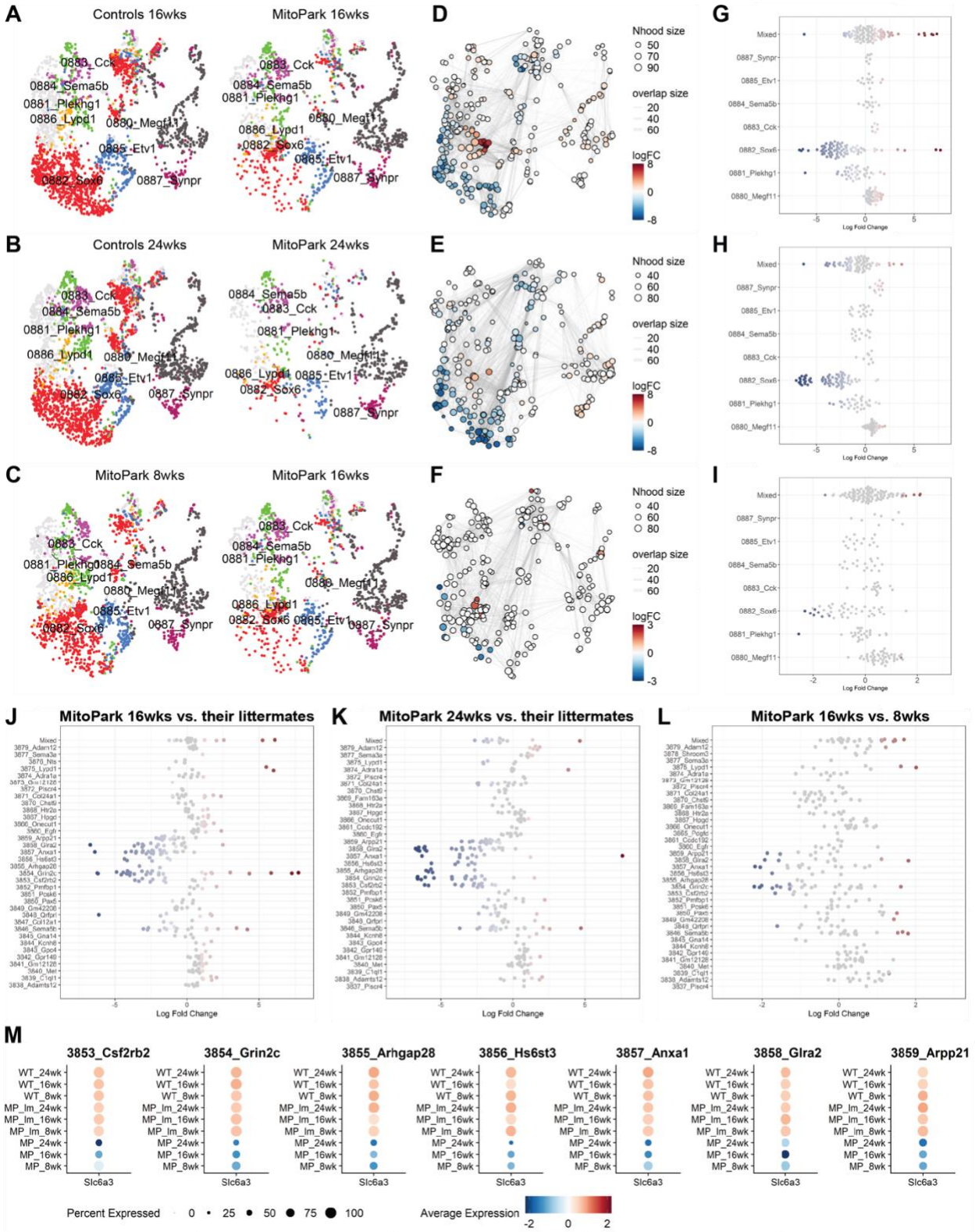

Extended Data Fig.7 Selective vulnerability of *Sox6*+ dopaminergic population revealed by differential abundance test with Milo, Related to Fig.4

1266 Differential abundance testing for the dopamine subpopulations with supertype annotations by
1267 the ABC atlas. **A-C.** UMAP plots showing the dopamine subpopulations of MitoPark mice and
1268 their controls. **D-F.** Neighborhood graphs with the results from Milo differential abundance
1269 analysis between MitoPark mice and their littermate controls (D:16 weeks, E: 24 weeks), and
1270 between MitoPark mice at different stage (F: 8 weeks and 16 weeks). **G-I**. Beeswarm plots
1271 showing the distribution of log-fold changes in each supertype group. Colors are represented
1272 similarly to **D-F**. **J-L**. Beeswarm plots showing the distribution of log-fold changes in each
1273 cluster. Colors are represented similarly to **Fig.4D-F**. **M**. Comparison of DAT expression
1274 among *Sox6*+ dopamine subtypes revealed no substantial differences.

Extended Data Fig.8

A

GO Table

Based on dopamine subcluster

Source	Term name	Term ID	Cluster	log10(1/padj)
GO:BP	nervous system development	GO:0007399	3854_Grin2c	85.68
GO:BP	neurogenesis	GO:0022008	3854_Grin2c	76.55
GO:BP	generation of neurons	GO:0048699	3854_Grin2c	74.69
GO:CC	cell junction	GO:0030054	3854_Grin2c	111.69
GO:CC	synapse	GO:0045202	3854_Grin2c	97.04
GO:CC	cytoplasm	GO:0005737	3854_Grin2c	79.54
GO:MF	protein binding	GO:0005515	3854_Grin2c	85.87
GO:MF	binding	GO:0005488	3854_Grin2c	33.21
GO:MF	ion binding	GO:0043167	3854_Grin2c	32.86
HP	Abnormal muscle tone	HP:0003808	3854_Grin2c	5.27
HP	Abnormal nervous system physiology	HP:0012638	3854_Grin2c	5.27
HP	Abnormality of mental function	HP:0011446	3854_Grin2c	4.99
KEGG	Axon guidance	KEGG:04360	3854_Grin2c	9.54
KEGG	Glutamatergic synapse	KEGG:04724	3854_Grin2c	8.91
KEGG	Morphine addiction	KEGG:05032	3854_Grin2c	8.70
MIRNA	mmu-miR-15a-5p	MIRNA:mmu-miR-15a-5p	3854_Grin2c	3.45
MIRNA	mmu-miR-340-5p	MIRNA:mmu-miR-340-5p	3854_Grin2c	3.33
MIRNA	mmu-miR-149-5p	MIRNA:mmu-miR-149-5p	3854_Grin2c	3.01
REAC	Neuronal System	REAC:R-MMU-112316	3854_Grin2c	19.47
REAC	Transmission across Chemical Synapses	REAC:R-MMU-112315	3854_Grin2c	10.89
REAC	Protein-protein interactions at synapses	REAC:R-MMU-6794362	3854_Grin2c	8.66
TF	Factor: ZF5; motif: GSGCGCGR; match class: 1	TF:M00716_1	3854_Grin2c	112.68
TF	Factor: ZF5; motif: GSGCGCGR	TF:M00716	3854_Grin2c	98.98
TF	Factor: ZF5; motif: NRNGNGCGCGCWN; match class: 1	TF:M00333_1	3854_Grin2c	95.72
WP	Dravet syndrome Scn1a A1783V point mutation model	WP:WP5298	3854_Grin2c	4.88
WP	Splicing factor NOVA regulated synaptic proteins	WP:WP1983	3854_Grin2c	3.98
WP	G protein signaling pathways	WP:WP232	3854_Grin2c	3.49

B

GO Table

Based on dopamine subcluster

Source	Term name	Term ID	Cluster	log10(1/padj)
GO:BP	nervous system development	GO:0007399	3855_Arhgap28	72.23
GO:BP	neurogenesis	GO:0022008	3855_Arhgap28	62.71
GO:BP	system development	GO:0048731	3855_Arhgap28	59.98
GO:CC	cell junction	GO:0030054	3855_Arhgap28	62.84
GO:CC	neuron projection	GO:0043005	3855_Arhgap28	59.86
GO:CC	synapse	GO:0045202	3855_Arhgap28	56.83
GO:MF	protein binding	GO:0005515	3855_Arhgap28	39.92
GO:MF	cytoskeletal protein binding	GO:0008092	3855_Arhgap28	19.07
GO:MF	binding	GO:0005488	3855_Arhgap28	18.82
HP	Tremor	HP:0001337	3855_Arhgap28	4.95
HP	Myoclonus	HP:0001336	3855_Arhgap28	3.86
HP	Involuntary movements	HP:0004305	3855_Arhgap28	3.84
KEGG	Morphine addiction	KEGG:05032	3855_Arhgap28	9.82
KEGG	Glutamatergic synapse	KEGG:04724	3855_Arhgap28	7.65
KEGG	GABAergic synapse	KEGG:04727	3855_Arhgap28	7.18
MIRNA	mmu-miR-758-3p	MIRNA:mmu-miR-758-3p	3855_Arhgap28	3.94
MIRNA	mmu-miR-425-5p	MIRNA:mmu-miR-425-5p	3855_Arhgap28	2.87
REAC	Neuronal System	REAC:R-MMU-112316	3855_Arhgap28	15.38
REAC	Transmission across Chemical Synapses	REAC:R-MMU-112315	3855_Arhgap28	9.58
REAC	Neurotransmitter receptors and postsynaptic signal transmission	REAC:R-MMU-112314	3855_Arhgap28	2.62
TF	Factor: Sp1; motif: GGNGGGGGNGGGGGMGGGGCNGGG	TF:M10375	3855_Arhgap28	33.09
TF	Factor: CTCF; motif: NAGGGGGCGCNNKNNNN; match class: 1	TF:M08995_1	3855_Arhgap28	27.03
TF	Factor: ZF5; motif: NRNGNGCGCGCWN; match class: 1	TF:M00333_1	3855_Arhgap28	25.14
WP	Dravet syndrome Scn1a A1783V point mutation model	WP:WP5298	3855_Arhgap28	5.10
WP	Dopaminergic neurogenesis	WP:WP1498	3855_Arhgap28	3.95
WP	Splicing factor NOVA regulated synaptic proteins	WP:WP1983	3855_Arhgap28	3.32

C

GO Table

Based on dopamine subcluster

Source	Term name	Term ID	Cluster	log10(1/padj)
CORUM	Sh3kbp1-Cblb-Egfr complex	CORUM:5172	3857_Anxa1	1.30
GO:BP	nervous system development	GO:0007399	3857_Anxa1	91.15
GO:BP	neurogenesis	GO:0022008	3857_Anxa1	83.86
GO:BP	system development	GO:0048731	3857_Anxa1	82.54
GO:CC	cell junction	GO:0030054	3857_Anxa1	113.87
GO:CC	synapse	GO:0045202	3857_Anxa1	99.92
GO:CC	neuron projection	GO:0043005	3857_Anxa1	89.89
GO:MF	protein binding	GO:0005515	3857_Anxa1	74.58
GO:MF	binding	GO:0005488	3857_Anxa1	32.25
GO:MF	ion binding	GO:0043167	3857_Anxa1	25.68
HP	Autistic behavior	HP:0000729	3857_Anxa1	7.33
HP	Abnormal communication	HP:0034434	3857_Anxa1	5.91
HP	Abnormality of speech or vocalization	HP:0002167	3857_Anxa1	5.58
KEGG	Axon guidance	KEGG:04360	3857_Anxa1	9.78
KEGG	GABAergic synapse	KEGG:04727	3857_Anxa1	9.63
KEGG	Glutamatergic synapse	KEGG:04724	3857_Anxa1	9.39
MIRNA	mmu-miR-758-3p	MIRNA:mmu-miR-758-3p	3857_Anxa1	2.53
MIRNA	mmu-miR-425-5p	MIRNA:mmu-miR-425-5p	3857_Anxa1	2.44
MIRNA	mmu-miR-9-5p	MIRNA:mmu-miR-9-5p	3857_Anxa1	2.41
REAC	Neuronal System	REAC:R-MMU-112316	3857_Anxa1	29.87
REAC	Transmission across Chemical Synapses	REAC:R-MMU-112315	3857_Anxa1	19.52
REAC	Neurotransmitter receptors and postsynaptic signal transmission	REAC:R-MMU-112314	3857_Anxa1	10.51
TF	Factor: ZF5; motif: GSGCGCGR; match class: 1	TF:M00716_1	3857_Anxa1	75.40
TF	Factor: ZF5; motif: GSGCGCGR	TF:M00716	3857_Anxa1	65.82
TF	Factor: ZF5; motif: NRNGNGCGCGCWN; match class: 1	TF:M00333_1	3857_Anxa1	63.72
WP	Dravet syndrome Scn1a A1783V point mutation model	WP:WP5298	3857_Anxa1	8.91
WP	Calcium regulation in cardiac cells	WP:WP553	3857_Anxa1	6.34
WP	Cholesterol biosynthesis	WP:WP103	3857_Anxa1	6.15

D

GO Table

Based on dopamine subcluster

Source	Term name	Term ID	Cluster	log10(1/padj)
CORUM	Caveolar macromolecular signaling complex	CORUM:384	3858_Glra2	1.31
CORUM	Caveolar macromolecular signaling complex, using anti-Cav-3	CORUM:385	3858_Glra2	1.31
GO:BP	system development	GO:0048731	3858_Glra2	32.92
GO:BP	generation of neurons	GO:0048699	3858_Glra2	32.89
GO:BP	neuron differentiation	GO:0030182	3858_Glra2	32.85
GO:CC	synapse	GO:0045202	3858_Glra2	57.14
GO:CC	cell junction	GO:0030054	3858_Glra2	53.72
GO:CC	neuron projection	GO:0043005	3858_Glra2	41.44
GO:MF	protein binding	GO:0005515	3858_Glra2	19.51
GO:MF	gated channel activity	GO:0022836	3858_Glra2	13.58
GO:MF	monoatomic ion channel activity	GO:0005216	3858_Glra2	12.19
HP	Epileptic encephalopathy	HP:0200134	3858_Glra2	1.66
KEGG	Axon guidance	KEGG:04360	3858_Glra2	8.92
KEGG	Oxytocin signaling pathway	KEGG:04921	3858_Glra2	6.14
KEGG	Aldosterone synthesis and secretion	KEGG:04925	3858_Glra2	5.31
REAC	Neuronal System	REAC:R-MMU-112316	3858_Glra2	17.64
REAC	Transmission across Chemical Synapses	REAC:R-MMU-112315	3858_Glra2	7.65
REAC	Axon guidance	REAC:R-MMU-422475	3858_Glra2	4.81
TF	Factor: CTCF; motif: NAGGGGGCGCNNKNNNN; match class: 1	TF:M08995_1	3858_Glra2	15.79
TF	Factor: ZF5; motif: NRNGNGCGCGCWN; match class: 1	TF:M00333_1	3858_Glra2	15.69
TF	Factor: FOXN4; motif: NNWANNCGWMCGCGTCNNNNMT; match class: 1	TF:M04662_1	3858_Glra2	15.56
WP	Splicing factor NOVA regulated synaptic proteins	WP:WP1983	3858_Glra2	5.19
WP	Calcium regulation in cardiac cells	WP:WP553	3858_Glra2	3.40
WP	Myometrial relaxation and contraction pathways	WP:WP385	3858_Glra2	2.58

Extended Data Fig.8 Gene Ontology (GO) enrichment analysis for vulnerable dopaminergic population, Related to Fig.4

1278 Enrichment analysis of gene ontology (GO) terms for key genes in a representative vulnerable
1279 dopamine cluster (A, 3854_Grin2c; B, 3855_Arhgap28; C, 3857_Anxa1; D, 3858_Glra2).

Extended Data Fig.9

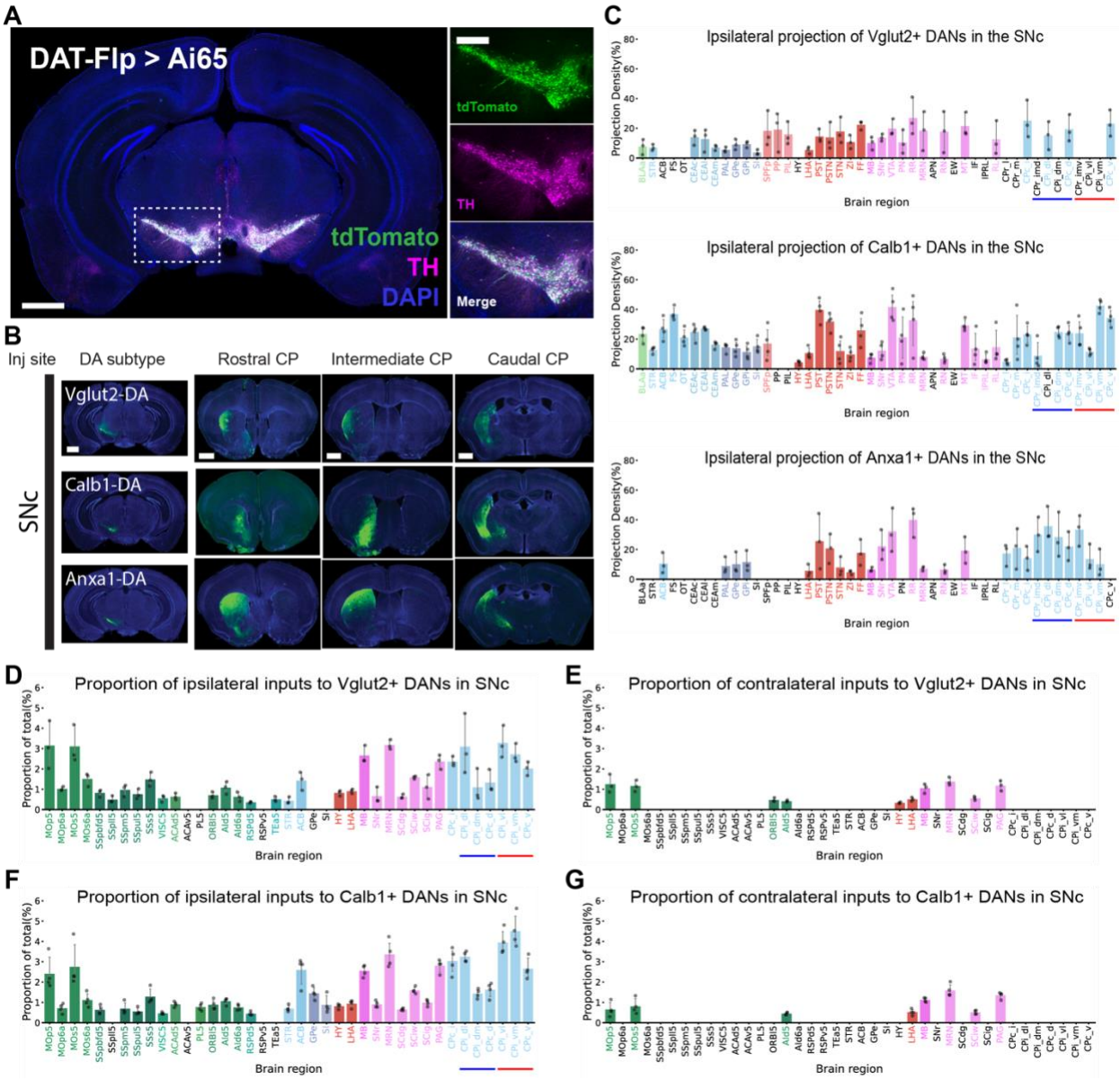

Extended Data Fig.9 Whole-brain efferent and afferent connectivity of dopaminergic neuron subtypes, Related to Fig.5

A. Characterization of the DAT-Flp line using a reporter line (Ai65) confirmed that tdTomato+ cells are *Th*+ neurons. Scale bars: 1mm for the striatum (left) and 400μm for the substantia nigra (right). **B.** Representative images of axonal projections of *Vglut2*+, *Calb1*+ and *Anxa1*+ dopamine neuron subtypes in the SNc. They preferentially project to dorsolateral striatum, ventral medial striatum and dorsal striatum. Scale bar 1mm. **C.** Brain regions to which *Vglut2*+, *Calb1*+ and *Anxa1*+ dopamine neuron project, measured as the fraction of neurites found within those brain structures defined Allen brain atlas (n=4 *Calb1*+ and n=3 for *Vglut2*+ and *Anxa1*+).

1290 Blue horizontal line indicates dorsal striatum and red line indicates ventral striatum. **D-G.**
1291 Statistical analysis of the whole-brain distribution of ipsilateral (left) or contralateral (right)
1292 monosynaptic inputs to *Vglut2*+ neurons (D, E) or *Calb1*+ dopamine neuron subtype (F, G) in
1293 the SNc. Brain areas are color-coded by the Allen Brain Atlas.

Extended Data Fig.10

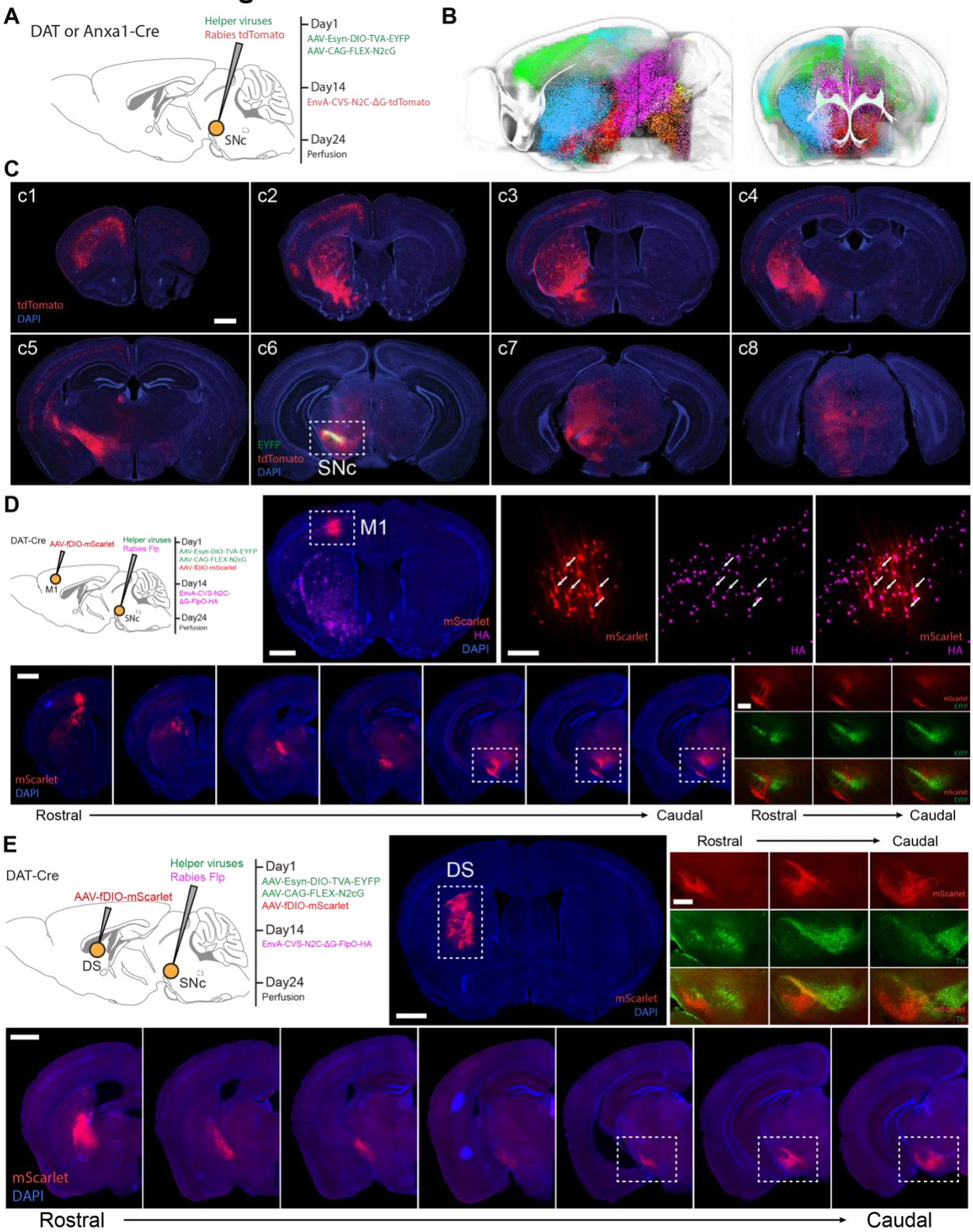

Extended Data Fig.10 Direct afferent inputs from the motor cortex or striatum to the SNc DANs, Related to Fig.5

1297 **A.** Schematic of the rabies injection procedure and experimental timeline for helper viruses and
1298 rabies viruses in the DAT-Cre or Anxa1-Cre. **B.** Whole-brain 3D reconstruction using BrainJ,
1299 color coded by brain regions[19] (left: sagittal view, right: coronal view). **C.** Representative images
1300 of monosynaptic inputs to DANs from the whole brain (c1-c8, from the rostral to caudal). The
1301 small white rectangle indicates the injection site, the SNc. Scale bar 1mm. **D-E.** Monosynaptic
1302 projections from primary inputs include cells associated with motor function to the SNc DANs
1303 (D, motor cortex; E, striatum). Scale bars: 1mm for the striatum and 400μm for the substantia
1304 nigra.

Extended Data Fig.11

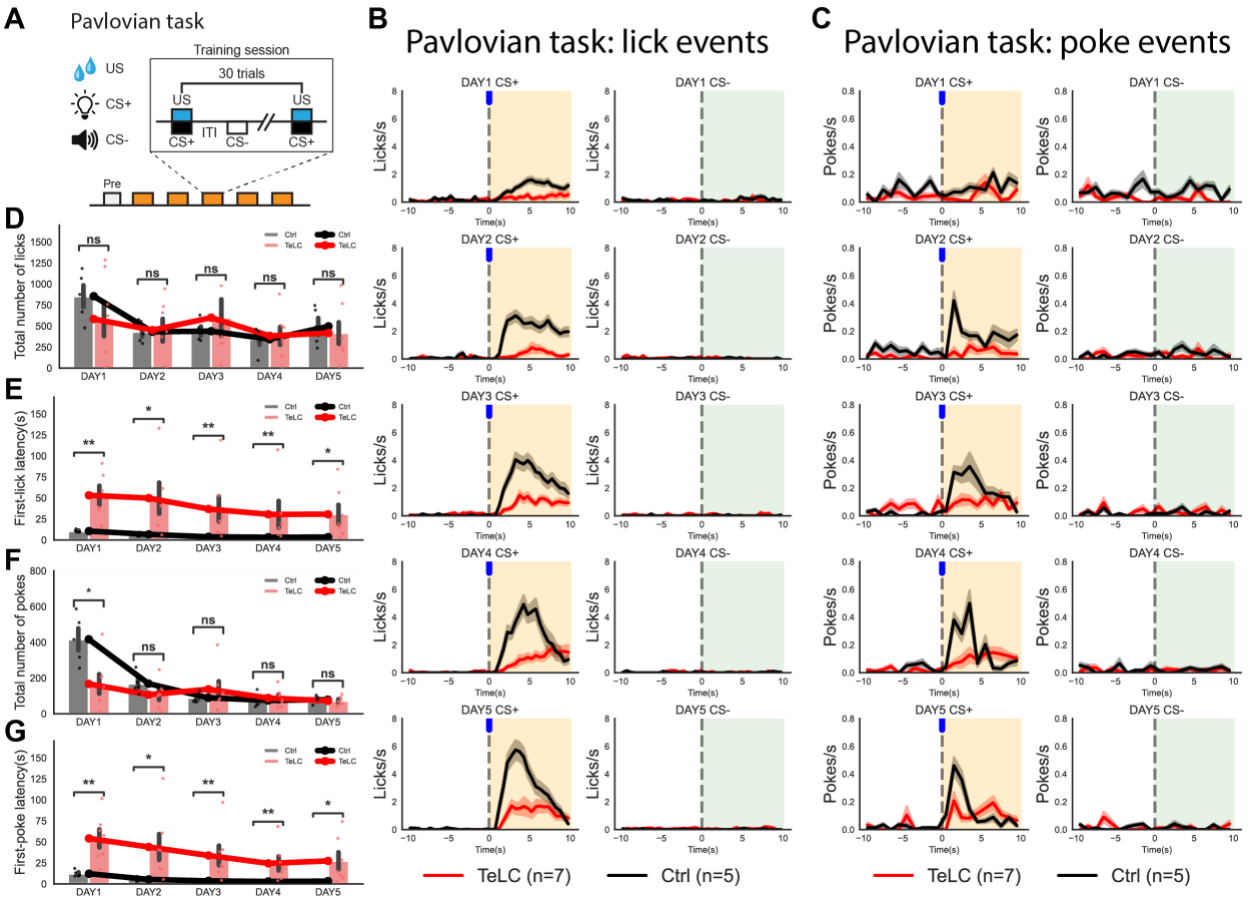

Extended Data Fig.11 Related to Fig.6

A. Schematic representation of the Pavlovian task. A light and a tone are used as CS+ and CS- respectively. **B-C.** PSTH (the peristimulus time histogram) of the lick or poke rate frequency of Anxa1-TeLC animals (red) and their controls (black) in response to CS+ (left) or CS- (right). The control animals consistently demonstrated a robust response to the light stimulus over time; in contrast, the Anxa1-TeLC animals exhibited a diminished response. D-G. Although the total number of licks did not differ significantly (D), there was a notable difference in the latency to the first lick between the Anxa1-TeLC and control animals (E). I-J. On Day 1, a difference in the number of pokes was observed, but this disparity did not persist in subsequent days (F). Additionally, there was a significant difference in the latency to the first poke between the mutant and control animals (G).